Helium and hydrogen effect on the microstructural evolution and mechanical property of irradiated Co-free FCC medium entropy alloys for nuclear application

Mengke NIU

Division of Materials Science and Engineering

Graduate School of Engineering

Hokkaido University

February 2025

Acknowledgements

At the end of my studies at Hokkaido University, I am deeply indebted to everyone who has supported me over the past three years, both academically and personally. PhD course has been a significant challenge for me, and I could not have completed it without the help and support of others.

First and foremost, I would like to express my heartfelt gratitude to my supervisor, Professor Naoyuki Hashimoto, for accepting me as his doctoral student. He provided immense support and constant encouragement for both my research and personal life. I have learned a great deal from his kind guidance and advice.

Secondly, I extend my sincere thanks to Professor Shigehito Isobe and Professor Hiroshi Oka for their unwavering guidance, insightful feedback, and consistent encouragement throughout my research. Their helpful communication has boosted my confidence and helped me solve many research problems.

I would also like to thank Secretary Kaori Kobayashi for her invaluable assistance with both my studies and daily life over the past three years. I am grateful to all the members of the LOAM group as well. Despite my limited Japanese, they were always patient and willing to help me, both in research and daily life in Japan, making my study abroad experience warm. I also would like to express my appreciation to the members of the laboratory of Nano-Mirco Materials Analysis (NMA) for their support on the use of instruments.

Special thanks go to my friends in Sapporo, who have provided great support since I arrived in Japan. I am particularly thankful to my friend Xu Fangfang for listening to

my troubles, encouraging mutual hard work, and providing companionship when I was down.

Lastly, I am deeply appreciative of my family, whose love and belief in me have been my foundation. Thank you to my parents for their endless love and encouragement. To my little sister and brother, thank you for bringing me joy.

This dissertation is a testament to the collective support and contributions of all these individuals. I am profoundly grateful to each one of you for helping me reach this milestone.

Abstract

The research and development of advanced nuclear power systems are critically important for the commercialization of next generation nuclear reactors. New structural materials with high corrosion and irradiation resistance are urgently required for extended use at high temperatures and high doses. In recent years, medium and/or high-entropy alloys (M/HEAs) have garnered significant attention due to their attractive mechanical properties. The high strength, ductility, and corrosion resistance make HEAs potential candidates for structural applications in high temperature fission or fusion reactors. Heavy ion irradiation has been intensively used to investigate the irradiation effects on HEAs including swelling, hardening, and phase stability. However, one of particular concern is the simultaneous production of helium and hydrogen that have a strong impact on the microstructure evolution of irradiated materials. Typically, they may cause additional swelling and embrittlement of materials. In this study, the performance of four different Cr-Fe-Mn-Ni HEAs under irradiation, including He and H effect on the microstructure evolution and mechanical properties, are also investigated.

Firstly, a group of Co-free medium entropy alloys(MEAs): $Cr_{0.65}FeMnNi$, $Cr_{0.8}FeMnNi$, $Cr_{0.8}FeMn_{1.3}Ni$, $Cr_{0.8}FeMn_{1.3}Ni_{1.3}$ were prepared by arc melting. After annealing at 1100 °C for 48 hours, the samples were cold-rolled, followed by recrystallization at 1000 °C for 4 hours. Electron backscattered diffraction (EBSD), tensile test and nano-indentation test was conducted to characterize the microstructure and the mechanical properties for each alloy. The elevated Mn content within this alloy induced a high atomic size difference within the material, inducing highest hardness and smallest grain size in $Cr_{0.8}FeMn_{1.3}Ni$. The high grain boundary strengening and solid

solution strengthening result in the high strength of $Cr_{0.8}FeMn_{1.3}Ni$.

Secondly, in order to understand He injection amount effect on the microstructure evolution in HEAs, $Cr_{0.8}FeMnNi$ and 316L were irradiated with Fe^{2+} at a temperature of 500 ℃ with different He^{+} preinjection amount. Transmission electron microscopy was used to characterize the irradiation-induced defects. As He injection amount increased, the binding energy of the self-interstitial atom (SIA) to the He-V complex decreased. This reduction result in the increase of the SIA in the matrix, affecting the evolution of point defects.

Thirdly, $Cr_{0.8}FeMnNi$ and 316L is irradiated with single beam (Fe^{3+}), dual beam (Fe^{3+}+He^{+}) and triple beam (Fe^{3+}+He^{+}+H^{+}) at 500 ℃. He and H effect on irradiation induced hardening and swelling on HEAs and 316L is studied. The nanoindentation test showed that MEAs showed higher irradiation hardening resistance than 316L. The microstructure characteration results indicates that under single beam irradiation, large cavities formed in $Cr_{0.8}FeMnNi$. Small bubbles with high density were found in dual and triple beam irradiated Cr0.8FeMnNi and 316L. He enhanced the nucleation and H can enhanced the growth of bubbles. The interaction bewteen He and vacancy could be weaker in $Cr_{0.8}FeMnNi$.

This work indicated that Mn content can affect the lattice distortion of MEA, affecting the microstructure and mechanical property. The pre-injected He amount can affect the binding energy of SIA to He-V cluster. The decrease of the binding energy of SIA to He-V complex can affect the point defect evolution. The bulk irradiation showed that He enhanced the nucleation and H can enhanced the growth of bubbles in MEAs.

Contents

List of figures

List of tables

Chapter 1

Introduction

1.1 New generation energy system

The development of the global economy and society requires substantial energy support. However, human production is still heavily dependent on fossil fuels. From Fig 1.1, fossil fuels like petroleum, coal, and natural gas still make up a large portion of today's energy system. Huge amounts of fossil fuels are utilized in electricity and car industry, which leads to severe environmental consequences, including air pollution, greenhouse gas emissions, and climate change. On a global scale, climate change has become more apparent and new fossil fuel reserves have become scarce. Considering this situation, it is essential to identify the effective transition from a fossil-fuel to a renewable energy-system.

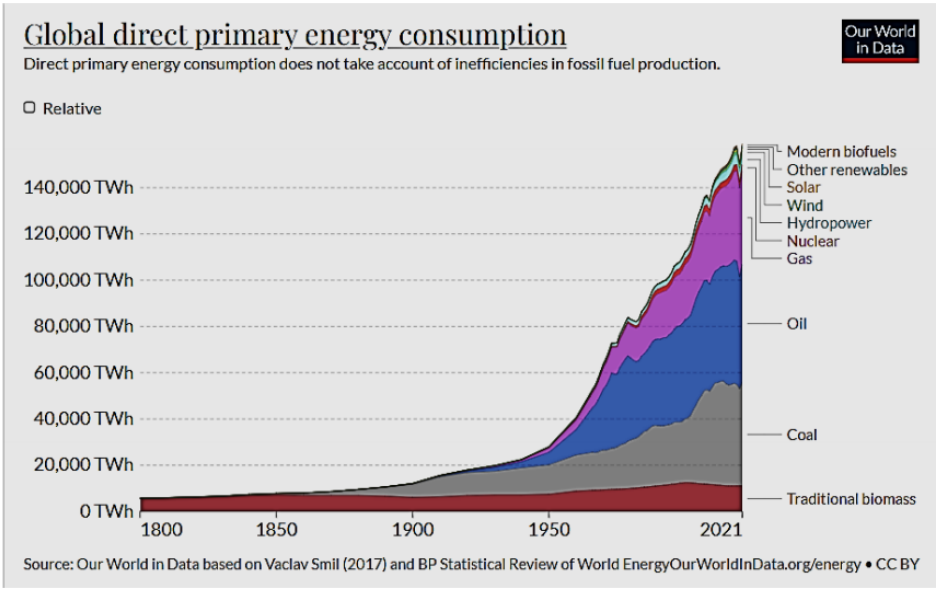

Fig 1.1 Primary energy consumption by the source of the world [1]

In recent years, the research about sustainable development has intensified, driven by the require of mitigating climate change, and ensuring energy security. These issues underscore the urgent need for a transition to cleaner energy sources. As technology develops, the efficiency of energy utilization has made great progress in developing renewable energy [1, 2]. Renewable energy is derived from natural sources that are constantly replenished, such as sunlight, wind, tides, and geothermal heat. Nuclear power is considered a clean and environment-friendly resource and has historically been one of the largest contributors of carbon-free electricity globally due to the very low carbon emission since energy generation currently accounts for 66% of greenhouse gas emission[3, 4]. According to the survey results, there are about 1/3 of the world's electricity production from fission and renewable energy by 2012 [5].

1.2 Nuclear energy development

Nowadays, more and more researchers have paid attention to nuclear energy due to its high production efficiency and environmentally friendly properties. Unlike fossil fuels, nuclear power can be obtained from nuclear fission and nuclear fusion reactions. The reactions could be described as[6, 7]:

$$n+U \rightarrow A+B+xn(0.1\text{-}1MeV) \quad (1\text{-}1)$$

$$D+T \rightarrow {}^4He(3.5MeV)+n(14MeV) \quad (1\text{-}2)$$

From the equations, it can be found that a huge amount of energy is released accompanied with no CO_2 or other harmful gas during the reaction This characteristic makes nuclear energy a powerful tool in reducing the carbon output of the energy system. Moreover, advancements in nuclear technology have significantly improved the safety, efficiency, and economic viability of nuclear power, making it a more attractive option for meeting future energy needs sustainably.

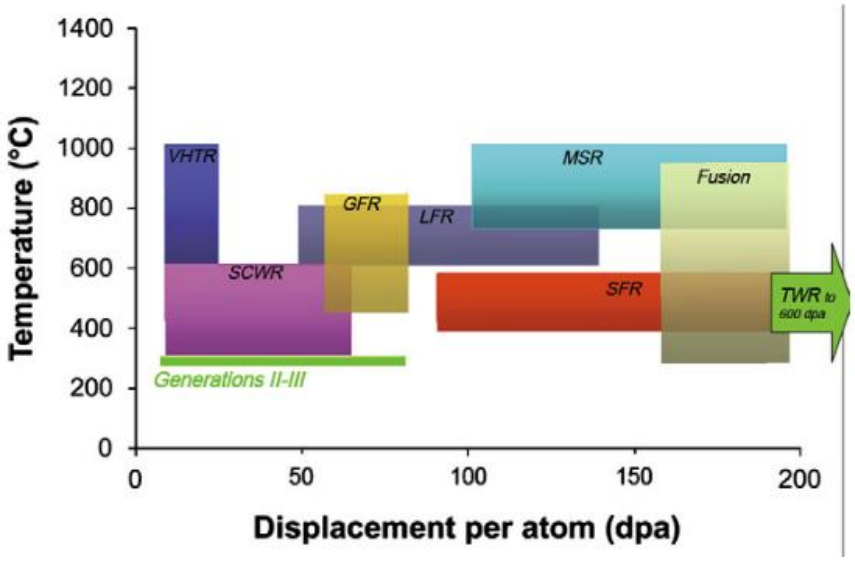

Fig 1.2 Temperature and dose requirements for in-core structural materials for the operation of the six proposed Generation IV advanced reactor concepts, the traveling wave reactor, and fusion reactor concepts. The dimensions of the colored rectangles represent the ranges of temperature and displacement damage for each reactor concept.[8]

Currently, nuclear energy systems have acquired extensive expertise through the operation of reactors from generation I to generation III, alongside the predominant design of water-cooled reactors[9]. Fig 1.2 shows the temperature and dose requirements for in-core structural materials for the operation of the six proposed Generation IV advanced reactor concepts [8].

The next generation of water-cooled nuclear reactors is strategically devised to enhance the efficiency inherited from previous iterations. Various aspects, including safety problems, operational efficiency, and power output are necessarily interlinked with their design. There are also various types of next-generation nuclear energy systems including the lead-cooled fast reactor (LFR), the gas-cooled fast reactor (GFR), the sodium-cooled fast reactor (SFR), the molten salt reactor (MSR), the supercritical-water-cooled reactor (SCWR), alongside more compact designs like the pebble bed reactor (PBR). These reactors require harsh environment with radiation doses of up to 100-200 displacements per atom (dpa) and outlet temperatures ranging from 550-850 ℃, and new corrosion problems are emerging both in MSR and SCWR[10].

Nuclear reactors present an exceptionally harsh environment for component materials service due to high fuel temperatures, intense radiation flux, and coolant compatibility issues. Therefore, the properties of nuclear reactor materials, such as the fuel, the cladding, the structural materials, the reactor vessel, and the interaction of these materials, must possess enhanced resistance to irradiation, swelling, relaxation, growth, and corrosion.

1.3 Structural materials in nuclear reactors

Structural materials in nuclear reactors are pivotal for ensuring safe, efficient, and long-lasting operation. It plays a key role in the containment of nuclear fuel and fission products as well as the thermodynamically efficient production of electrical energy from nuclear reactors. Similarly, the performance of structural materials is critical for the future success of proposed fusion energy reactors, which will subject the structures to unprecedented fluxes of high-energy neutrons along with intense thermomechanical stresses.

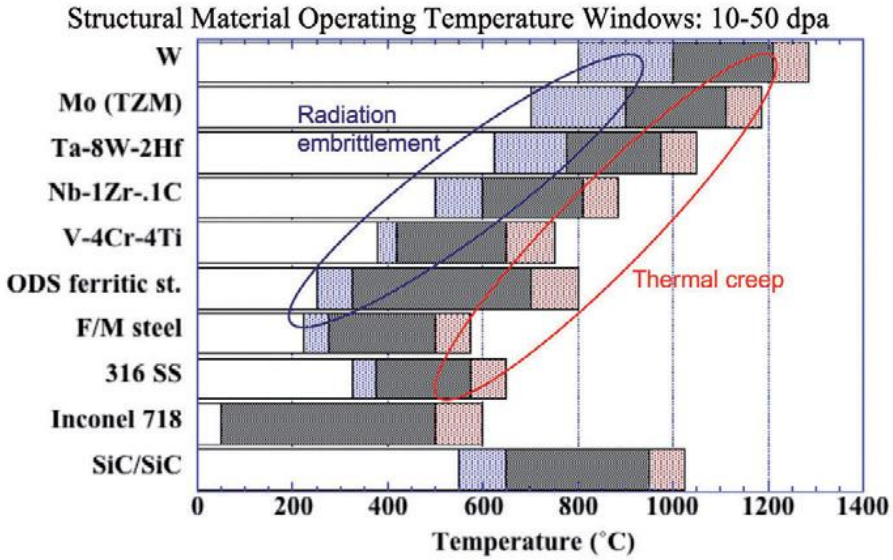

Fig 1.3 Estimated operating temperature windows (dark shaded region) for structural materials in nuclear energy systems for damage levels of 10 to 50 dpa. The light blue and red regions represent lower and upper temperature uncertainty bands[11].

Some candidate materials for innovative reactor systems have been intensively investigated. Fig 1.3 shows some existing structural materials, which have rather limited operating temperature regimes where they can be utilized in a neutron irradiation environment for moderate damage levels of 10 to 50 dpa [11, 12]. At low temperature, the ductility reduction caused by low temperature radiation hardening will greatly threaten the safety of the reactor [13]. In cases where fracture toughness is reduced by low temperature irradiation, the operating temperature is restricted to higher temperatures. The upper operating temperature limit is typically determined by thermal creep strength or high temperature helium embrittlement considerations.

Some structural materials have been deeply investigated during the past few decades. Ferritic/martensitic steels (9–12% Cr) are one of the most promising candidate materials for sodium or lead cooled reactors with a high temperature (<875 K) and compact primary system, as well as for the pressure vessel of high temperature gas-cooled reactors. They are also considered core structure materials of fusion reactors. Oxide dispersion-strengthened ferritic/martensitic steels are considered for cladding materials for high burn-up fast neutron reactor fuels, which show excellent irradiation resistance. However, the under-irradiation stability of the oxide dispersion is an open issue to be settled. Ceramic materials are needed for very high temperature components (>1275 K) such as heat exchangers and thermal insulations in the primary system, as well as core components. The major aspect of research about ceramics is the

development of brittle ceramics forms such as composite ceramics, or nano-structured plastic ceramics [14].

Through former studies, it can be found that each structural material has its advantages and disadvantages and is suitable for different types of reactors. The structural materials for advanced nuclear systems need to endure much higher neutron doses, higher temperatures, and extremely corrosive environment, which are beyond the performances of materials used in current nuclear systems. The design and development of the new generation of structural materials should have excellent mechanical properties, oxide resistance, and irradiation resistance properties, which have important significance for solving the material bottleneck problem and improving the long-term safe and stable operation of nuclear power plants.

1.4 High entropy alloys

1.4.1 Resent progress about HEAs

Researchers previously focused on designing conventional alloys, which occupy a small part of designing space[15]. With the advent of HEAs, HEAs have been considered as the potential nuclear materials used for future fission or fusion reactors, which are designed to operate at higher temperatures and higher radiation doses up to several hundreds of displacement per atom (dpa) [16].

The definition of HEAs is based on either composition or the magnitude of entropy [17-19]. In contrast to traditional alloys, as equi-atomic or approximately atomic, multi-element metallic systems, HEAs are defined as those alloys having four or more principal metallic elements, each with an atomic percentage between 5% and 35%[17]. Recently, some minor elements (usually below a 5% atomic percentage) have also been added to the HEAs to further optimize the properties[20-23]. Under the entropy definition, HEAs are defined as those alloys having a configuration entropy larger than 1.5 R [R (= 8.31 J/K·mol) is the gas constant] [24-26]. The multiple elements with different crystal structures can crystallize as a relatively simple phase, i.e., face-centered cubic (fcc), body-centered cubic (bcc), or hexagonal close-packed (hcp)[27]. The phase stability (at high enough temperatures) against phase separation and formation of intermetallic phases result from the high mixing entropy, which could be achieved when the number of elements was large enough and the stoichiometry was close to equiatomic. These element combinations make the combinations of tunable

properties that would be hardly possible in conventional alloys, such as high hardness, strength and ductility, oxidation resistance, etc[19, 28]. The attractive physical and mechanical properties of HEAs make them potential candidates for high temperature fission or fusion structural applications [29-32].

Mechanical properties are strongly dependent on microstructure and composition. Composition sets out atomic interactions and elastic properties that determine dislocation behaviors. Due to the unique elemental composition, high-entropy alloys possess complex high entropy effects, which result in excellent mechanical properties.

1.4.2 High entropy effect

Sluggish diffusion, lattice distortions, and the cocktail effect constitute the core effects of HEAs, [19, 33, 34], which have been assumed to be responsible for the excellent properties of HEAs.

Recent research has suggested that phase transformation and diffusion kinetics in high-entropy alloys (HEAs) are slower than those in conventional alloys. The presence of multiple principal elements in nearly equimolar ratios creates a highly complex atomic environment. Each atom is surrounded by a diverse set of neighboring atoms, resulting in a wide variety of bonding interactions and local energy states [35]. In kinetics, the sluggish diffusion effect of HEAs could lower the diffusion rate of atoms and thus the phase transformation rate in the multielement matrix (or the whole solute matrix) of a phase.

As Fig 1.4 shows, compared to the periodic arrangement of atoms in conventional materials, the varying atomic sizes of different elements in high-entropy alloys lead to significant lattice distortion [25]. This phenomenon significantly influences the properties of HEAs, not only affecting microstructure and properties but also affecting thermodynamics and kinetics. For example, higher lattice distortion could impede dislocation movement, resulting in solid solution strengthening.

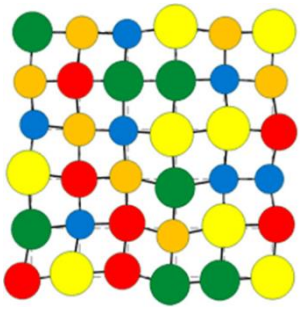

Fig 1.4 Severely distorted lattice in a multielement crystal structure[25]

For metallic alloys, the cocktail effect indicates that unexpected properties can be obtained after mixing various elements, which could not be obtained from only one independent element. The cocktail effect for metallic alloys was first mentioned by Ranganathan [36], which has been subsequently confirmed in the mechanical and physical properties. This effect indicates that the mechanical properties can be greatly optimized by adjusting the composition and alloying

The core effects of high-entropy alloys influence many aspects of physical metallurgy. The sluggish diffusion effect lowers the diffusion rate and phase transformation rate, thus affecting kinetics in phase transformation. The severe lattice distortion effect not only affects deformation theory and all the relationships among each property, structure, and microstructure but also affects thermodynamics and kinetics. The cocktail effect is the overall effect on properties from composition, structure, and microstructure. The investigation of these effects would be helpful to find out the mechanism of the excellent mechanical properties of HEAs.

1.4.2 Irradiation resistance of HEAs

Currently, irradiation studies have been conducted on HEAs, most of which are CoCrFeMnNi-type high-entropy alloys. In nuclear reactors, structural materials will suffer from irradiation. Irradiation effects, including irradiation hardening, irradiation embrittlement, irradiation creep, and irradiation fatigue, could significantly affect the mechanical properties of nuclear materials. Among these effects, irradiation-induced hardening and embrittlement are two crucial mechanical property characteristics of concern in the safety assessment of nuclear energy systems.

As Fig 1.5(a), (b) illustrated, the stress-strain curves and yield strengths of a single-crystal Ni, and binary alloys, NiCo, NiFe, and NiCoFeCr HEA, under different irradiation doses are obtained. Under low irradiation doses, the NiFe alloy and NiCoFeCr HEA have the same excellent radiation resistance. When the radiation dose increased to 53 dpa, the NiCoFeCr HEA showed the most excellent irradiation-hardening resistance than other alloys. From Fig 1.5(c), the radiation-hardening resistance of HEAs is stronger than that of traditional alloys.

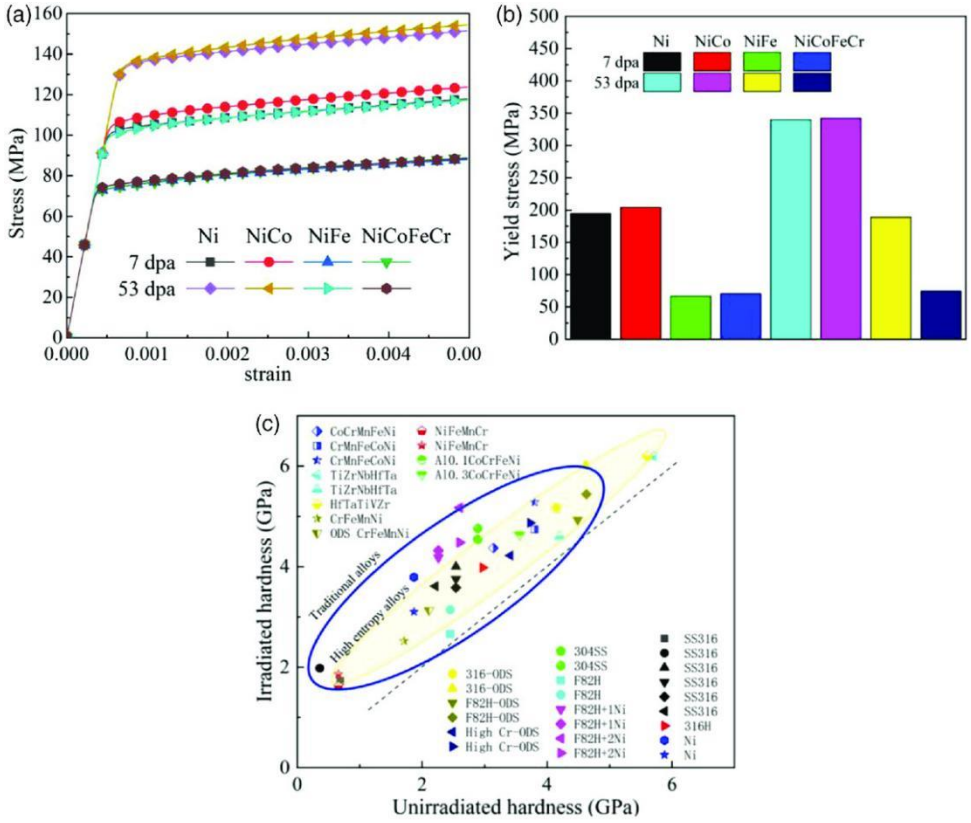

Fig 1.5 (a) Stress-strain curve; (b) yield strength of Ni, NiCo, NiFe, and NiCoFeCr under different irradiation doses; (c) Unirradiated hardness and irradiated hardness of traditional alloys and HEAs (the closer to the dotted line, the smaller the degree of radiation hardening) Severely distorted lattice in a multielement crystal [37-40].

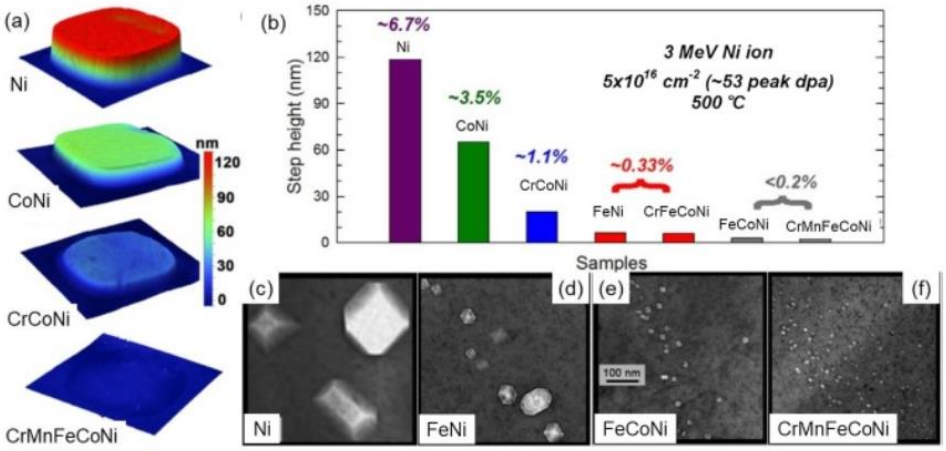

Fig 1.6 (a) Optical profilometer measurements of void swelling in Ni, CoNi, CrCoNi, and CrMnFeCoNi. (b) Step height change of each alloy after irradiation. Cross-sectional TEM images showing different sizes and density of voids in (c) Ni, (d) CoNi, (e) CrCoNi, and (f) CrMnFeCoNi [41].

Fig 1.6 shows the extent of swelling measured using an optical profilometer and

corresponding cross-sectional TEM images of voids in Ni, CoNi, FeNi, CrCoNi, FeCoNi, CrFeCoNi, and CrMnFeCoNi irradiated with 3 MeV Ni ions to 5 × 1016 cm−2 (peak dose 53 dpa) at 773 K. All six alloys exhibited significantly lower void swelling than Ni. The void swelling of Ni was 6.7% whereas CrMnFeCoNi and FeCoNi showed the lowest void swelling of < 0.2%, and was approximately similar for the FeNi[41, 42].

From the above research, it can be observed that high entropy alloys exhibit excellent radiation resistance in both microstructure and mechanical properties. The enhanced resistance to irradiation in HEAs can be attributed, to the sluggish diffusion and lattice distortion of HEAs. These effects play a significant role in immobilizing irradiation-induced point defects and impeding the clustering of defects [43].

1.5 Research on helium irradiation in metal materials

Helium is produced in nuclear fission and fusion energy systems by transmutation reactions in amounts ranging from less than one to thousands of atomic parts per million (appm), depending on the neutron spectrum, fluence, and alloy composition. Neutron scattering generates primary recoiling atoms (PRAs), which in turn, generate a branching cascade of recoiling atoms that are displaced from lattice sites. Cascades contain a high local concentration of vacancy and SIA point defects, along with small defect clusters, that typically form complexes with alloy solutes[44]. Fig 1.7 schematically illustrates the combined effects of He and displacement damage on irradiation-induced microstructural evolutions [44].

The primary characteristic of He is that it is essentially insoluble in solids. Hence, in the temperature range where it is mobile, He diffuses in the matrix and initially precipitates as bubbles, typically at various microstructural trapping sites, including dislocations, grain boundaries, and precipitate interfaces [45]. Fig 1.7(d) shows that He precipitates to form bubbles (larger blue circles) at various sites, in this case in the matrix. Fig 1.7(e) shows that when bubbles reach a critical size they convert to unstably growing underpressurized voids (large orange circle containing blue He atoms) due to an excess flux of vacancies over SIA arising from the dislocation bias for the latter defect. Fig 1.7(f) shows the corresponding growing creep cavities transformed from critical He bubbles on stressed GBs.

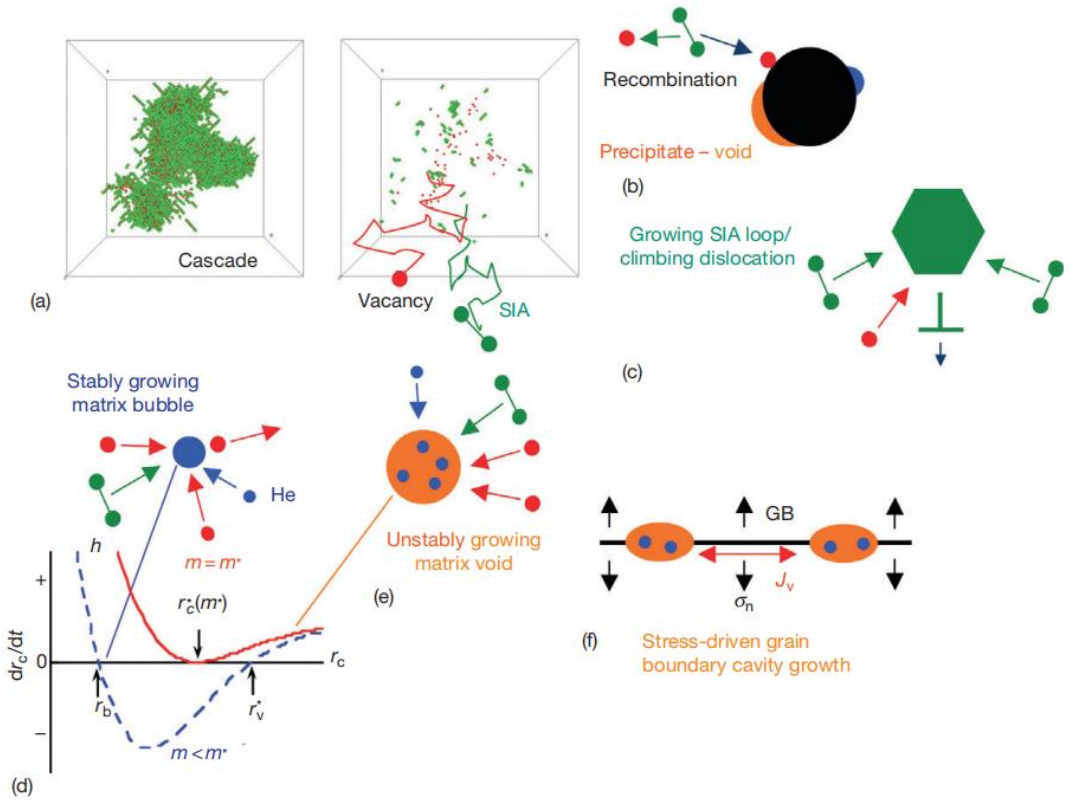

Fig 1.7 Illustration of the combined effects of He and displacement damage on irradiation-induced microstructural evolutions [45].

These bubbles can serve as nucleation sites of growing voids in the matrix and creep cavities on grain boundaries (GBs), driven by displacement damage and stress, respectively. While helium effects are primarily manifested as variations in cavities, all microstructural processes occurring under irradiation are intrinsically coupled. Therefore, differences in the helium generation rate can also affect the evolution of precipitates, dislocation loops, and network dislocations.

Fig 1.8 illustrates the effects that seriously affect the safety of reactor structural materials at different temperatures. At high temperatures, He can further degrade the tensile ductility and the other high temperature properties, primarily by enhancing grain boundary cavitation [46]. At intermediate temperatures, growing voids form on He bubbles, and He accumulation largely controls the incubation time before the onset of rapid swelling [47, 48]. High He concentrations can also extend irradiation hardening and fast fracture embrittlement to intermediate temperatures [49]. At lower temperatures, high He concentrations enhance large positive shifts in the ductile-to-brittle transition temperature (DBTT) [50, 51].

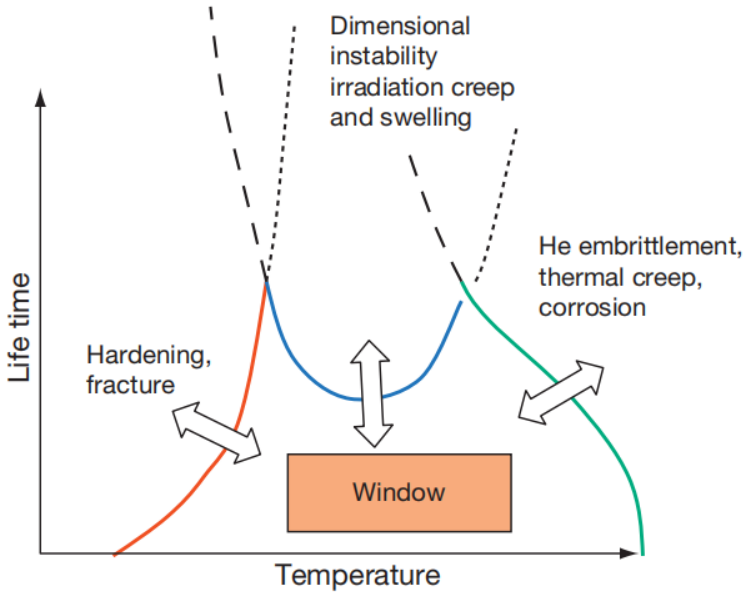

Fig 1.8 Illustration of the materials design window for the fusion energy environment, as a function of temperature [52].

According to research about He effect on the structural materials, helium produced by nuclear reactions can significantly alter the microstructure of materials, leading to changes in mechanical properties and overall performance. The understanding of helium interacts with materials under irradiation is essential for the development of more durable and resilient materials for nuclear reactors. By studying these effects, researchers can design materials that better withstand the harsh conditions of irradiation, improving the safety and longevity of nuclear reactors.

1.6 Objective of this study

The development of next-generation nuclear systems for higher efficiency and longer lifetime requires new structure materials with enhanced properties of corrosion and radiation resistance. HEAs have been considered as the potential nuclear materials used for future fission or fusion reactors due to their excellent mechanical properties and high irradiation resistance.

Current extensive research on the irradiation effect, such as phase stability, irradiation hardening, and void swelling, provides the basis for the study of the irradiation resistance of high-entropy alloys (HEAs). CoCrFeMnNi is one structurally simple equiatomic HEA, exhibiting single-phase with FCC crystal structure, which has attracted both practical and scientific interests from a few perspectives. However, the

presence of Co poses a significant challenge in post-neutron-irradiation testing, since Co would be highly activated by neutron irradiation [53, 54], and produce ^{60}Co radioisotope during irradiation. $Cr_{0.8}FeMnNi$ alloy has excellent mechanical properties and does not have high-activation elements, so it offers significant advantages in nuclear energy system applications.

Considering the significant effect of He on the performance of structural materials, a series of FCC Cr-Fe-Mn-Ni HEAs was investigated inn this work. By conducting various irradiation experiments on this series of materials, the properties of these materials after irradiation were studied, especially the evolution of irradiation defects. It is hoped that through this work, the mechanism of He effect on the microstructure evolution of irradiation-induced defects in HEAs can be investigated.

Chapter 2

Experiment methodology

2.1 Preparation of materials

2.1.1 Arc melting

Various processing methods have been employed to fabricate HEAs. HEAs have been produced in the form of castings, thin films, powder metallurgy parts, and many others. Arc melting and induction heating are generally utilized to produce alloys from different elements that require high-melting temperature, especially for arc-melting, inside temperature can reach more than 3000℃. Arc melting, particularly the vacuum arc melting (VAM) method, has been one of the most prominent melt processing methods for HEAs fabrication due to its ability to reach the high temperatures required for melting the constituent metals.

Fig 2.1 Arc melting furnace with an enclosed crucible.

As shown in Fig 2.1, the heating process is done by the electrical arc between a tungsten electrode and metals placed in a crucible in a copper core. In the melting process, the chamber is evacuated first and then filled with argon gas. Since Ar is an inert gas that does not react with molten metal, the evacuation of the chamber prevents the oxidation of the melt alloys. The heat produced by the electric arc between the electrode and the metals is used to melt the metals placed in the crucible to create an alloy. The melting process will be repeated several times to increase the homogeneity of the alloy.

In this study, pure Cr, Fe, Mn, and Ni (>99.99% purity for each) were used as raw elements material for the fabrication of the face-centered cubic Co-free Cr-Fe-Mn-Ni single-phase concentrated solid-solution alloys. All HEAs ($Cr_{0.65}FeMnNi$, $Cr_{0.8}FeMnNi$, $Cr_{0.8}FeMn_{1.3}Ni$, $Cr_{0.8}FeMn_{1.3}Ni_{1.3}$) were made by arc-melting under a high purity Ar atmosphere, with the ingot turned and melted for more than four times to achieve complete melting and increase the homogeneity of all alloys.

2.1.2 X-ray fluorescence (XRF) spectrometry

X-ray fluorescence (XRF) is a non-destructive analytical technique used to determine the elemental composition of materials. In XRF test, materials are irradiated with high-energy X-rays, causing the atoms within the material to emit secondary (fluorescent) X-rays. These emitted X-rays have energies characteristic of the compositional elements in the material. XRF analyzers determine the chemistry of a sample by measuring the fluorescent (or secondary). The program that includes data on each element of the periodic table is then used to pick the possible elements contained in the sample and to identify the amount using their individual energies. In this study, after preparing the material using the ARM method, the XRF technique was used to determine the elemental composition of the material.

Fig 2.2 X-ray Fluorescence Spectroscopy (JEOL / JSX-3100RII).

2.1.3 X-ray diffraction

X-ray diffraction (XRD) is a nondestructive technique which has been widely used to study the crystal structure of materials. Diffraction occurs when light is scattered by a periodic array with long-range order, producing constructive interference at specific

angles. The atoms in a crystal are periodically arranged thus diffracting light. The wavelengths of X-ray are similar to the distance between atoms, XRD techniques use this principle to elucidate the crystalline nature of materials. The scattering of X-rays from atoms produces a diffraction pattern that contains information about the atomic arrangement in the crystal.

XRD is widely used in materials science, chemistry, geology, and biology to identify unknown crystalline materials, determine the crystal structure and phase composition, and study the crystallographic properties and quality of the material. The target materials of this paper are FCC single phase high entropy alloys, to ensure that the prepared material is a single phase alloy, XRD method is used to conduct structural analysis of the material to ensure that no second phase is generated in the material.

Fig 2.3 The figure of SmartLab XRD.

2.2 Irradiation experiment

To efficiently evaluate irradiation resistance, ion irradiation has been widely used to substitute neutron irradiation [55].

In this study, to investigate He/dpa ratio effect on the microstructure evolution on $Cr_{0.8}FeMnNi$ and 316L stainless steel, helium atoms were injected, followed by Fe^{2+}

irradiation at various He/dpa ratios. The pre-injection of He^{+} was performed at room temperature with a Multi-beam High-Voltage Electron Microscope (HVEM) at Hokkaido University. Heavy ion irradiation was conducted by using the High Fluence Irradiation Facility at the University of Tokyo (HIT).

In addition, $Cr_{0.8}$FeMnNi, $Cr_{0.65}$FeMnNi, and 316L were irradiated with single beam (Fe^{3+}), dual beam(Fe^{3+}+He^{+}), and triple beam (Fe^{3+}+He^{+}+H^{+}) at 500°C in Takasaki Ion Accelerators for Advanced Radiation Application(TIARA). The irradiation hardening effect and microstructure evolution were characterized to investigate He effect on MEAs.

2.3 Characterization of material properties

2.3.1 Scanning electron microscopy (SEM)

Scanning electron microscopy (SEM) is a common technique that utilizes electrons to characterize the material's microstructure, surface morphology, and chemical distribution is scanning electron microscopy (SEM). Electrons emitted from an electron gun and focused into a fine beam raster across the surface of the samples. The signals generated by electron-sample interactions are collected by detectors and processed to create detailed images of the sample's surface. SEM provides high-resolution images that reveal surface topography, texture, and composition. It is widely used in materials science, biology, geology, and engineering for applications such as analyzing microstructures, assessing surface coatings, and investigating material failures.

SEM-EDX is a powerful analytical technique used to investigate the elemental composition of materials. By combining scanning electron microscopy (SEM) with energy-dispersive X-ray spectroscopy (EDX), SEM-EDX can visualize the microstructure of samples at high resolution while simultaneously identifying and quantifying the elements present.

Fig 2.4 The figure of scanning electron microscopy (SEM).

For the FCC MEAs in this research, the samples were studied using a scanning electron microscope (SEM, JSM-6510LA) equipped with a 15 kV accelerating voltage energy dispersive spectrometer (EDS) to characterize the element distribution and the morphology of fracture surface.

2.3.2 Electron backscatter diffraction (EBSD)

Electron Backscatter Diffraction (EBSD) is a technique used to analyze the crystallographic orientation and microstructure of materials. It operates on the principle that when a focused electron beam interacts with a crystalline sample, electrons are backscattered with different intensities depending on the crystallographic orientation. EBSD detects these backscattered electrons and uses them to determine the crystallographic orientation of individual grains in the sample.

EBSD is valuable for studying the microstructure of materials because it provides detailed information about the crystallographic orientation and spatial arrangement of grains within a sample. This information is essential for understanding the mechanical, thermal, and electrical properties of materials, as well as for optimizing manufacturing processes and designing new materials with tailored properties.

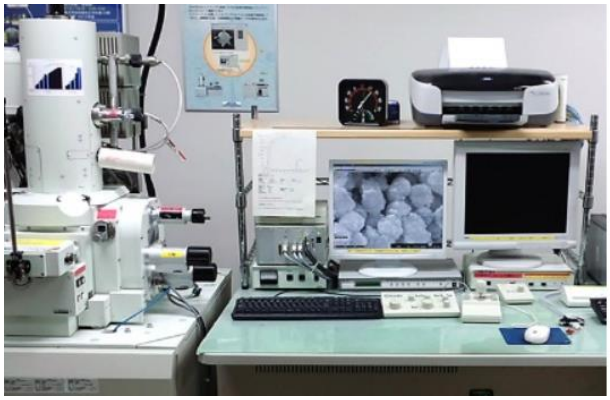

Fig 2.5 The figure of Electron Backscatter Diffraction (EBSD) facility.

2.3.3 Transmission electron microscopy (TEM)

Transmission Electron Microscopy (TEM) is a powerful technique used to observe the microstructure of materials at the atomic and molecular levels. It operates on the principle of transmitting a beam of electrons through a thin specimen, where the electrons interact with the sample to produce an image. TEM allows for the visualization of features such as crystal defects, dislocations, grain boundaries, and phase boundaries with extremely high resolution.

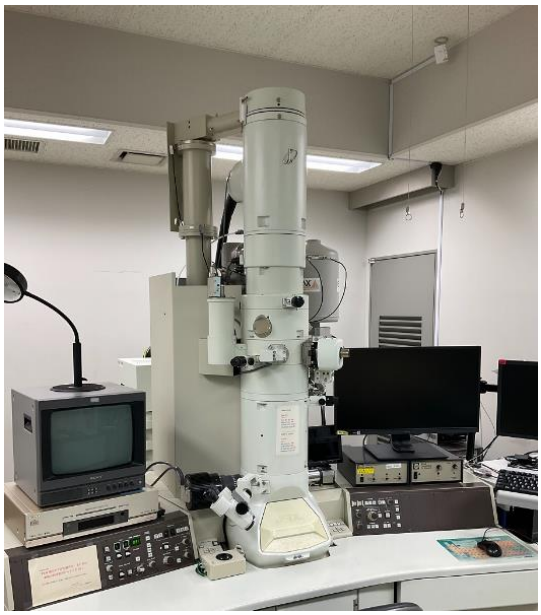

Fig 2.6 The figure of TEM(JEOL JEM-2010).

In this work, TEM is used to characterize the irradiation induced defects, including voids, He bubbles, and black dots. The irradiated sample was picked up into a strip using a FIB (Hitachi, FB-2100), and then thinned into a thin film which has a thickness of about 100-180 nm using an FIB (JEOL, JIB-4601F). Due to the different

crystallographic orientations and structures of various parts of a crystal, when characterizing a crystal using TEM, the samples are tilted to satisfy the Bragg condition. The common imaging modes observed in TEM mainly include two-beam dynamic condition, kinematic bright-field imaging (KBF), and weak-beam dark-field imaging [56, 57].

Fig 2.7 The figure of FIB (JEOL, JIB-4601F) facility.

(1) Observation of irradiation induced defects

In general, diffraction contrast does not satisfy the projection requirement because the bright-field (or dark-field) image intensity varies rapidly and in a complex way with sample orientation and thickness. Dislocations inclined to the electron beam give rise to images with intensity variations that change with crystal orientation. Such complicated intensity variations are not amenable to tomography and so. In the case of WBDF imaging, the diffraction contrast yields an image of a dislocation, which is narrow in width and close to the dislocation core. WBDF imaging is particularly effective for studying low-density crystal defects that may not be readily visible in conventional bright-field TEM images. By selectively enhancing the contrast of specific crystal defects, WBDF imaging enables researchers to gain insights into the formation, evolution, and behavior of these defects.

(2) Convergent beam electron diffraction (CBED)

The analysis of convergent-beam electron diffraction patterns for foil thickness is

easily carried out in the two-beam approximation to dynamical diffraction theory. Fig 2.8 shows the selection of typical two-beam dynamic conditions patterns taken from a copper sample using a (220) reflection [58]. The values of S_i, are determined by measuring the distance $\Delta\theta_i$ from the center of the diffracted beam profile to each of the successive minima, together with the distance $2\theta_d$ between the center spot and the diffracted spot. The value of $2\theta_d$ can be obtained by measuring the distance between corresponding positions on the image of the condenser aperture that defines each spot.

The thickness t of the foil sample could be obtained by measuring $\Delta\theta_i$ and $2\theta_d$ measurements via the equation,

$$S_i = \frac{\lambda}{d^2}\left(\frac{\Delta\theta_i}{2\theta_d}\right) \quad (2\text{-}1)$$

$$\left(\frac{S_i}{n_i}\right)^2 + \left(\frac{1}{n_i^2}\right)\left(\frac{1}{\xi_g^2}\right) = \frac{1}{t^2} \quad (2\text{-}2)$$

where λ is the wavelength and d is the spacing of the operating reflection, ξ_g is known to be sufficient accuracy.

In this work, CBED method was used to get the thickness of the observed area for each irradiated sample to calculate the number density of irradiation induced defects

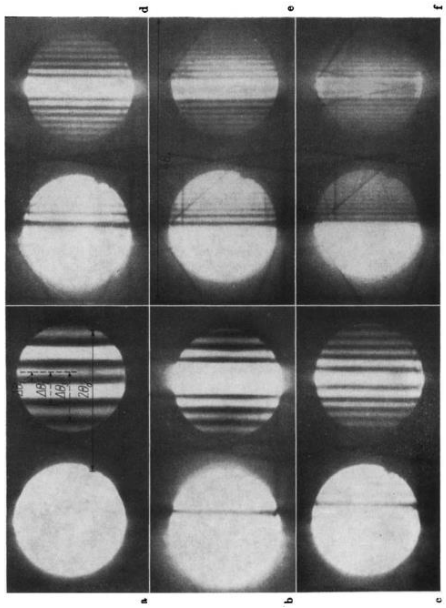

Fig 2.8 Two-beam (220) convergent beam diffraction patterns from a copper foil of varying thicknesses: (a) 550 8 Å, (b) 793 Å, (c) 1068 Å, (d) 1478 Å, (e) 1942 Å, (f) 2415 Å [58].

2.3.4 Mechanical property characterization

For as-cast samples, tensile test and nanoindentation test were used to compare the strength of each Cr-Fe-Mn-Ni high entropy alloy. The fracture surface of tensile samples is SEM observed to deeper investigate the mechanism of the strengthening of MEAs.

Nano-indentation was tested by G200 Agilent Tech with a Berkovich tip. Through the hardness at 200 nm and 300 nm in the irradiated and unirradiated areas of MEAs, the irradiation hardening effect was characterized to compare the irradiation resistance of Cr-Fe-Mn-Ni high entropy alloys.

Fig 2.9 Nanoindentation test machine(left) and tensile test machine(right).

Chapter 3

Microstructure and mechanical properties of Co-free Cr-Fe-Mn-Ni high entropy alloys

3.1 Introduction

In recent years, medium and/or high-entropy alloys (M/HEAs) have garnered significant attention due to their attractive mechanical properties. The high strength, ductility, and corrosion resistance make HEAs potential candidates for structural applications in high temperature fission or fusion [18, 28, 59]. HEAs are composed of four or more metallic elements mixed in an equimolar or near equimolar ratio [60]. High configurational entropy of mixing in these systems effectively suppresses intermetallic formation and results in a high degree of lattice strain from the presence of different sized atoms in the unit cell [61, 62].

CoCrFeMnNi is one structurally simple equiatomic HEA, exhibiting single-phase with FCC crystal structure. Initially investigated in 2004 by Cantor et al., this alloy has attracted both practical and scientific interests from a few perspectives. However, Co would be highly activated by neutron irradiation and produce ^{60}Co radioisotope during irradiation, which poses a significant challenge in post-neutron-irradiation testing. Therefore, HEAs that do not contain high-activation elements such as Co need to be developed as low-activation materials. Cr-Fe-Mn-Ni medium entropy alloy has excellent properties to CoCrFeMnNi alloy and does not have high-activation elements, so it offers significant advantages in nuclear energy system applications.

FCC-type materials (316SS, Cu-alloys, and Ni-base alloys have lower stacking fault energies (SFE) and tend to form stacking fault-type defects, such as stacking fault tetrahedron (SFT) and Frank loops (FLs) in the matrix [63-66]. Those stacking fault-type defects would increase the yield strength and decrease the elongation of materials, resulting in material degradation. Therefore, the control of SFE would be significant for FCC-type materials under irradiation. Previous studies theoretically estimated the SFE is affected by the content of Mn [67-69]. However, there is insufficient research on the mechanical properties of this MEA system, and the effect of varying principal element contents on microstructure and mechanical properties remains unclear. Apart from stacking fault energy, other influencing factors such as mechanical properties should also be taken into consideration in this MEA system. Therefore, this study investigated the effect of Mn content on the microstructure and mechanical properties of Cr-Fe-Mn-Ni MEAs.

3.2 Materials and methods

Four Cr-Fe-Mn-Ni MEAs $Cr_{0.65}FeMnNi$, $Cr_{0.8}FeMnNi$, $Cr_{0.8}FeMn_{1.3}Ni$, $Cr_{0.8}FeMn_{1.3}Ni_{1.3}$ were fabricated using commercially high purity metals (> 99.9 % purity). The ingots were prepared by argon (Ar) gas-protected arc-melting method with pure titanium as the oxygen getter. The ingots were flipped over and melted more than five times to ensure the homogeneity of the alloy. Subsequently, the as-cast alloys were homogenized at 1100 ◦C for 48 hours. Fig 3.1 shows the phase diagram calculated with the CALPHAD methodology, which is a phenomenological approach for calculating/predicting thermodynamic, kinetic, and other properties of multicomponent materials systems. It is expected that the phase of MEAs used in this work have FCC structure at annealing temperatures (1100 °C). The composition of the materials was determined using X-ray Fluorescence Spectroscopy (XRF) method (XRF, JEOL / JSX-3100R II). The chemical compositions and heat treatment conditions of these alloys are listed in Table 3.1. Then, the samples were cold-rolled to reduce the total thickness by 80%, followed by recrystallization at 1000 °C for 4 hours. All the heat-treatments were conducted by individually-encapsulated samples in evacuated quartz tubes.

Table 3.1 Chemical composition of the investigated alloys.

Element (at.%)	Cr	Fe	Mn	Ni
$Cr_{0.65}FeMnNi$	17.67	26.95	27.39	28.00
$Cr_{0.8}FeMnNi$	20.78	26.47	26.42	26.33
$Cr_{0.8}FeMn_{1.3}Ni$	19.26	24.15	32.44	24.15
$Cr_{0.8}FeMn_{1.3}Ni_{1.3}$	18.23	22.78	29.63	29.36

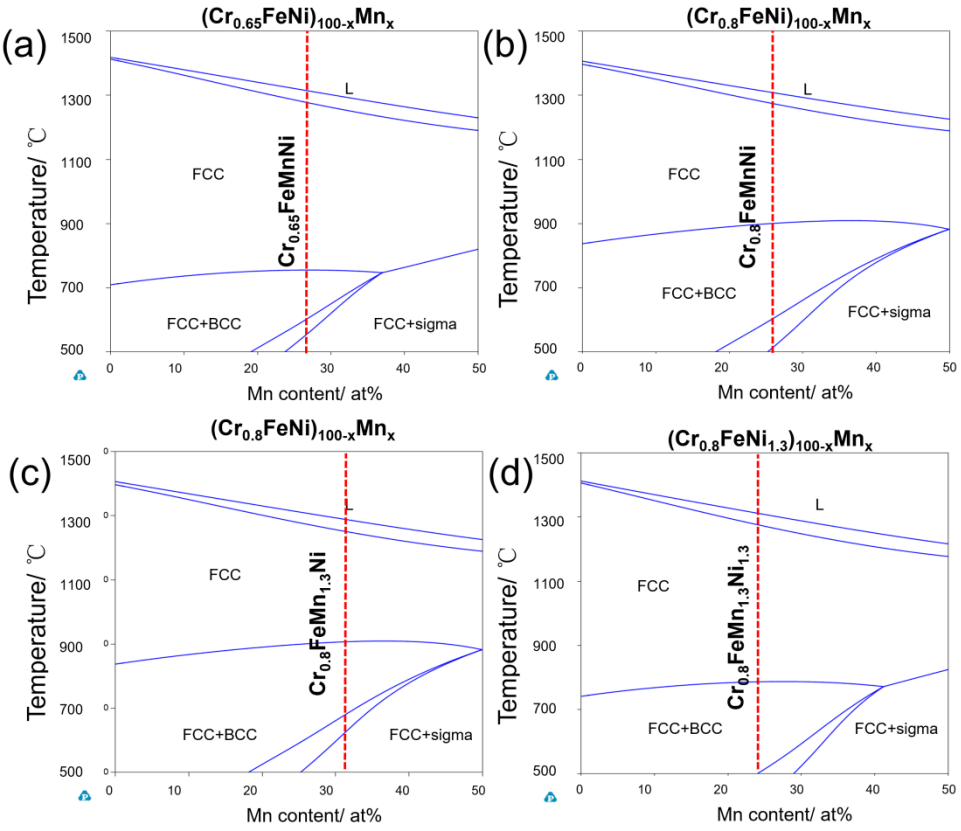

Fig 3.1 Phase diagrams of (a) $Cr_{0.65}FeMnNi$, (b) $Cr_{0.8}FeMnNi$, (c) $Cr_{0.8}FeMn_{1.3}Ni$, (d)$Cr_{0.8}FeMn_{1.3}Ni_{1.3}$ calculated with the CALPHAD methodology.

The fabricated samples were grounded using SiC paper, followed by mechanical polishing (#2000 and diamond spray of 1 μm). The phase constitutions of the specimens were characterized using X-ray diffraction (XRD, Rigaku SmartLab) at a speed of 6°/min with 75 Cu K_α radiation on a Rigaku Smart Lab. The microstructure was observed by scanning electron microscope (SEM, JSM-6510LA) equipped with an energy dispersive spectrometer (EDS) with an accelerating voltage of 15 kV. The grain sizes were determined through electron backscattered diffraction (EBSD, JEOL, JSM-6500F). Additionally, "dog-bone-shaped" tensile specimens, featuring a gauge length of 5 mm × 1.2 mm × 0.25 mm (length × width × thickness), were subjected to testing using an Instron 5564 testing system at a strain rate of approximately 10^{-3} s^{-1}. Furthermore, the fracture morphology of the tensile specimen was examined by SEM. Nanohardness tests were conducted at the depths of 200 nm and 300 nm using a nanoindentation tester (Hysitron TI 950) with a Berkovich-type indentation tip. At least 9 typical indents were conducted on each area with a distance of 15 μm which was

larger than five times the largest indentation diameter so that the hardness will not be affected by other indents.

3.3 Results and discussion

3.3.1 Microstructure and mechanical property analysis

According to the calculated phase diagram, all fabricated alloys should be FCC single-phase structure at 1100 ℃. The crystal structure illustrated in Fig 3.2 obtained by XRD analysis revealed that no evident secondary phase precipitation formed after homogenization at 1100 ◦C for 48 hours. Then the microstructure and mechanical properties are characterized by EBSD, nano-hardness test, and tensile test. The results are shown in Table 3.2.

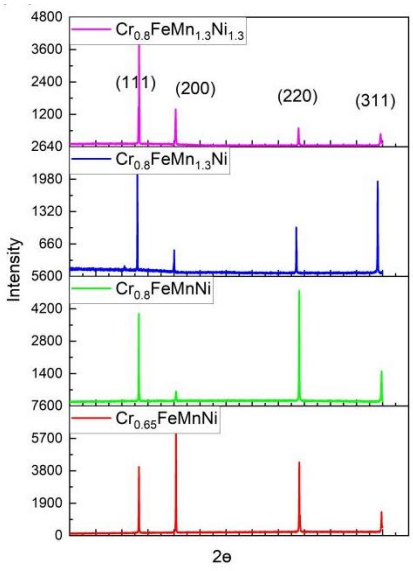

Fig 3.2 The crystal structures of Cr-Fe-Mn-Ni system MEAs.

Table 3.2 The information about the microstructure and mechanical properties of Cr-Fe-Mn-Ni system MEAs.

Materials	Mn (at%)	Atomic size mismatch δ	Dislocation density / m^{-2}	Everage grain size /μm	Hardness (300 nm) / GPa	Yield Strength /MPa
$Cr_{0.65}FeMnNi$	27.39	3.686	9.9×10^{12}	88.4	1.53±0.06	160±14
$Cr_{0.8}FeMnNi$	26.42	3.634	7.6×10^{12}	120.9	1.49±0.06	178±17
$Cr_{0.8}FeMn_{1.3}Ni$	32.44	3.822	10.6×10^{12}	28.1	2.49±0.09	208±15
$Cr_{0.8}FeMn_{1.3}Ni_{1.3}$	29.63	3.752	6.1×10^{12}	88.4	2.20±0.10	134±7

Fig. 3.3 shows the inverse pole figures for Cr-Fe-Mn-Ni MEA. ∑3 twin boundaries(60°<111>) marked with red lines can be observed in MEAs. The average grain size of $Cr_{0.8}FeMn_{1.3}Ni$ is much smaller than the other alloys. The average grain size of each alloy is shown in Fig 3.4. $Cr_{0.8}FeMn_{1.3}Ni$ exhibited the smallest average grain size of 28.1 μm. The geometrically necessary dislocations (GND) density for each alloy is also obtained using EBSD. Since the alloys were fully recrystallized, the dislocation densities in each alloys are low and with same order.

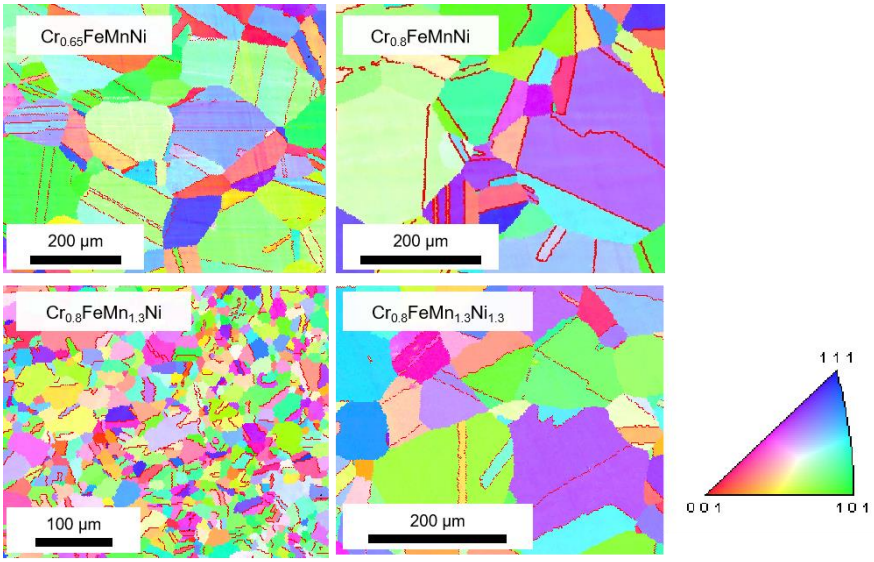

Fig 3.3 Inverse pole figures of (a) $Cr_{0.65}FeMnNi$, (b) $Cr_{0.8}FeMnNi$, (c) $Cr_{0.8}FeMn_{1.3}Ni$, (d) $Cr_{0.8}FeMn_{1.3}Ni_{1.3}$.

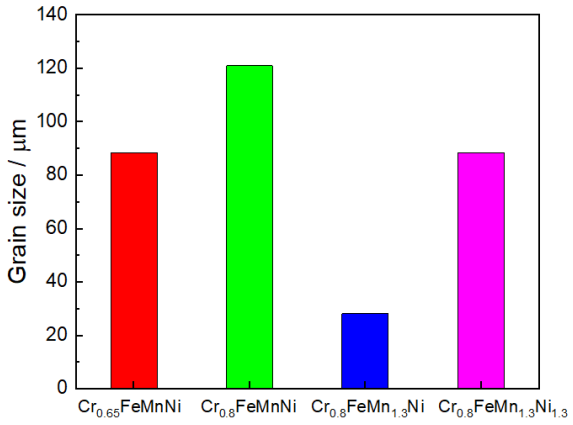

Fig 3.4 The average grain size of Cr-Fe-Mn-Ni MEAs.

Fig 3.5 shows the nano-hardness at different depths at room temperature for Cr-Fe-Mn-Ni MEA. The hardness of the samples was measured by G200 Agilent Tech with a Berkovich tip. At both depths of 200 and 300 nm, hardness increased with higher Mn

amount. Notably, $Cr_{0.8}FeMn_{1.3}Ni$ MEA exhibited the largest hardness at both 200 μm and 300 μm. It is important to note that in this study, the indentation size of nano-hardness test is significantly smaller than the average grain size, thereby the hardness difference is not influenced by average grain size.

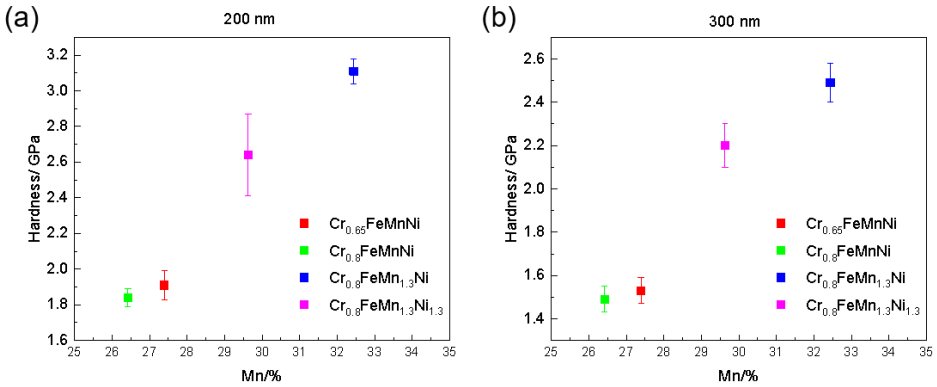

Fig 3.5 The nanohardness at the depth of (a) 200 nm and (b) 300 nm for Cr-Fe-Mn-Ni MEAs.

EBSD results reveal that Cr-Fe-Mn-Ni alloys show different grain size after same fabrication. The driving force for recrystallization is the amount of stored energy within the material. This energy arises from the lattice strains and the crystalline imperfections generated in the material during deformation processing. The bulk of the energy generated during the deformation of a metallic material is dissipated as heat with only a small fraction of the energy stored in the material [70]. Grain growth also referred to as normal grain growth or continuous grain growth normally sets in after the primary recrystallization, as the growing recrystallization nuclei begin to impinge on one another. It is characterized by the growth of some new grains at the expense of other newly formed grains resulting in a microstructure with a narrow range of grain size and shape [71, 72].

Tensile test was performed using an Instron 5564 testing system at a strain rate of approximately 10^{-3} s^{-1}. Fig 3.6(a) showed the stress versus strain and the fracture surface of the tensile test samples, as observed by SEM. Both the $Cr_{0.8}FeMn_{1.3}Ni$ and $Cr_{0.8}FeMn_{1.3}Ni_{1.3}$ samples exhibit ductile fracture surfaces. However, the ductile dimples of the fracture varied in size, which might attributed to the differences in grain size. Fig 3.6(b) illustrated the ultimate tensile strength(UTS) and yield strength of Cr-Fe-Mn-Ni MEAs and $Cr_{0.8}FeMn_{1.3}Ni$ showed the largest UTS and yield strength.

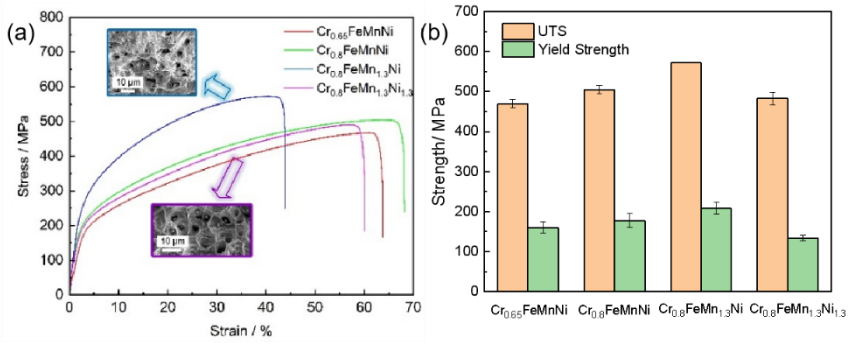

Fig 3.6(a) The stress-strain curve and (b) the average UTS and yield strength of Cr-Fe-Mn-Ni MEAs.

3.3.2 The relationship between the elements content and Mechanical properties

In M/HEAs, the formation of a solid solution is facilitated as each component could function as a solute atom, and each atom has the same probability of occupying the crystalline lattice. Generally, when a solute atom is introduced into a lattice, it induces a stress field in its surroundings due to the resulting local dilation or constriction of the lattice. Under an applied strain, the hardness (H) reflects the ability to resist localized plastic deformation, which is determined by the interaction energy of the solute atom with the dislocation, before the gliding takes place [73-76].

The expected level of strain is often related to the magnitude of the variation in atomic radii. A common method to assess strain level is through the evaluation of atomic size difference δ using the following expression,

$$\delta = \sqrt{\sum_{i=1}^{n} c_i \left(1 - \frac{r_i}{\bar{r}}\right)^2} \quad (3\text{-}1)$$

where n is the number of principal elements, r_i, and c_i are the atomic radius and atomic percentage [76] of i_{th} element, respectively, $\bar{r}$ is the average atomic radius [77-79]. The calculation result is shown in Table 3.2. Fig 3.7(a) illustrated that the atomic size difference increased with Mn content. As the Mn element possesses a larger atomic size, the incorporation of Mn atoms into the matrix may induce severe lattice distortion. The severe lattice distortion effect of M/HEAs could increase lattice strain, thereby enhancing the solid solution strengthening effect of the alloy system [80]. Consequently, the relatively larger atomic size of Mn may induce higher lattice distortion, leading to increasing resistance to deformation when external forces are applied. As a result,

elevated Mn content may contribute to heightened hardness, as illustrated in Fig 3.7(b).

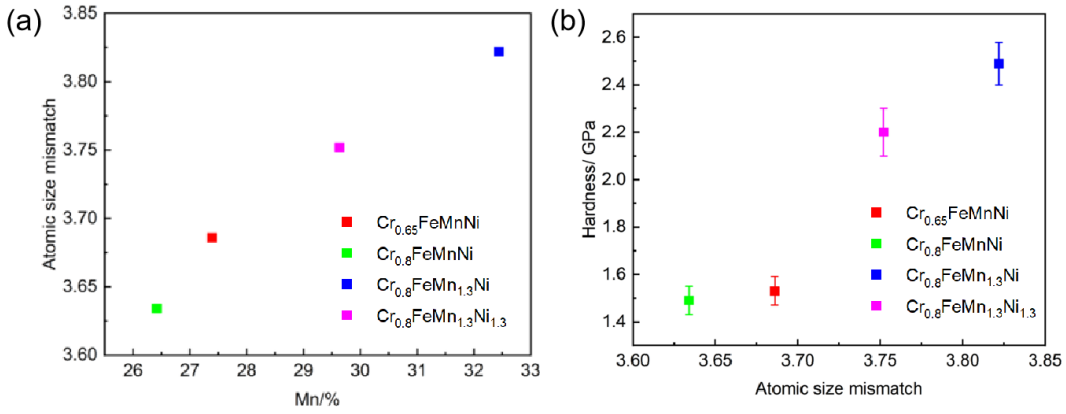

Fig 3.7 The relationship between (a) atomic size difference vs Mn content and (b) Hardness vs atomic size difference.

As shown in Fig 3.5, the grain size of the MEAs in this work is different. Some research about HEAs indicates that discontinuous recrystallization was observed in HEAs, and HEAs had shown strong resistance to the grain growth compared to traditional alloys [81, 82]. The special component of HEAs results in a low stacking fault energy (SFE), which promotes the deformation of twins during cold working and increases the nucleation sites for new grains during annealing. Meanwhile, the high lattice distortion increases the lattice friction stress against the motion of a dislocation line, resulting in slow grain boundary migration and difficulty of dislocation movement. In this work, as Fig 3.7(a) showed, the increase of Mn content leads to the increase of lattice distortion, enhancing the motion of dislocations and grain boundaries. Therefore, the average grain size of MEAs varies with Mn content.

In general, the strengthening mechanisms of metals or alloys mainly consist of grain boundary strengthening (σ_{gb}), solid solution strengthening (σ_{ss}), second phase particle strengthening (σ_{sp}), and dislocation strengthening (σ_{ds}), expressed as follows [83-88]:

$$\sigma = \sigma_{ss} + \sigma_{gb} + \sigma_{sp} + \sigma_{ds} \quad (3\text{-}2)$$

Solid solution strengthening involves the addition of alloying elements into the metal matrix, forming a solid solution. The solute atoms cause lattice distortions due to their different size and electronic structure compared to the host atoms. These distortions impede the motion of dislocations, thereby increasing the strength of the metal. One empirical equation has been widely used in many research [89], the relationship between the hardness and yield strength could be expressed as below:

$$\sigma_y = k\Delta H_V \quad (3\text{-}3)$$

where both σ_y and H_v are expressed in units of kg/mm^2, K values varies with materials. A linear relationship H_V= 0:86 H_0 was obtained between Vickers Meyer hardness H_v and bulk-equivalent nanoindentation hardness H_0 [90]. According to this relationship, it could be found that higher nanoindentation indicates higher solid solution strengthening. By this relationship, the liner relationship can also be found between yield strength and nanohardness. In this work, since the nanoindenter size is much smaller than the average grain size, the nanohardness only contains the effect of solid solution. According to this relationship, it could be found that higher nanoindentation indicates higher solid solution strengthening. Since the high Mn content results in the larger lattice distortion in $Cr_{0.8}FeMn_{1.3}Ni$, it shows the highest hardness among this for HEAs, which indicates the largest solid solution strengthening in $Cr_{0.8}FeMn_{1.3}Ni$.

Grain boundary strengthening relies on reducing the grain size of the metal. For polycrystalline materials, the grain boundary strengthening and average grain size follow the Hall-Petch behavior,

$$\sigma_{gb} = \sigma_0 + k_y/\sqrt{d} \quad (3\text{-}4)$$

where σ_{gb} is the 0.2% offset yield strength and σ_0 is a material constant, k_y is the Hall–Petch slope and d is the average grain size [91-93]. According to Hall-Petch behavior, materials with smaller grain sizes typically exhibit higher strength. Therefore, the grain boundary strengthening of $Cr_{0.8}FeMn_{1.3}Ni$, which has the smallest grain size, is the highest. However, $Cr_{0.8}FeMnNi$ shows larger yield strength compared to $Cr_{0.65}FeMnNi$. The average grain size in the previous manuscript is the result including twin boundaries. Some research has revealed that large-angle grain boundaries are effective barriers to dislocations, making deformation difficult and resulting in noticeable hardening. However, the strengthening effect of twin boundaries is highly dependent on their orientation. While twin boundaries can significantly strengthen bulk materials when twin boundary density is sufficiently high, there are situations where twin boundaries do not significantly affect the material's behavior [94]. Therefore, the yield strength seems inconsistent with grain size.

Also known as strain hardening or cold working, dislocation strengthening involves deforming the metal plastically, which increases the density of dislocations within the material, as shown below,

$$\sigma_d = \alpha M G b \sqrt{\rho} \quad (3\text{-}5)$$

where α is a constant, M is the Taylor factor, G is the shear modulus of the matrix, b is the magnitude of the Burgers vector, and ρ is the dislocation density. The dislocation density shown in Table 3.2 revealed the densities of four MEAs in the same order of magnitude, thus dislocation strengthening in this work has little effect on the difference in tensile strength.

Second phase particle strengthening is the strengthening caused by fine, dispersed particles within the metal matrix. These particles hinder dislocation movement, significantly improving the strength and hardness of the alloy. The heat treatment at 1000 ℃ will not induce second phase as the phase diagram shown. The XRD results also indicate no second phase generated in all the samples. Thus, second phase particle strengthening is not included in these alloys.

The high solid solution strengthening caused by high Mn content and large grain boundary strengthening due to the smallest average grain size, result in the high tensile property of $Cr_{0.8}FeMn_{1.3}Ni$.

3.4 Summary

This section analyzed the microstructure and mechanical properties of Cr-Fe-Mn-Ni medium entropy alloys (MEAs). Notably, $Cr_{0.8}FeMn_{1.3}Ni$ exhibits impressive hardness and strength compared with other MEAs.

The elevated Mn content within this alloy induced a high atomic size difference within the material. Such a pronounced atomic size difference could result in high lattice strain and small grain size. The heightened hardness is attributed to the enhanced solid solution strengthening, which is induced by higher lattice strain. This alloy also demonstrates the highest strength, attributed significantly to the smaller grain size, which greatly enhanced the resistance against deformation of grain boundary. By comparing the mechanical properties of different Cr-Fe-Mn-Ni MEAs and delving into the effect of Mn content, this study could serve as a reference point for adjusting material composition to optimize material properties effectively.

Chapter 4

Effect of He injection amount on the microstructural evolution in ion-irradiated MEA

4.1 Introduction

In recent years, medium and/or high-entropy alloys (M/HEAs) have garnered significant attention due to their attractive mechanical properties. $Cr_{0.8}$FeMnNi alloy has excellent mechanical properties and does not have high-activation elements, so it offers significant advantages in nuclear energy system applications.

To efficiently evaluate irradiation resistance, ion irradiation has been widely used to substitute neutron irradiation [55]. Helium(He), a primary by-product of neutron irradiation, exhibits interactions with vacancies that profoundly influence structural evolution [55]. Heavy ion irradiation has been intensively applied to HEAs, focusing on the swelling, hardening, phase stability, and many different aspects of HEA alloys [41, 95, 96]. Concurrently, numerous investigations by other researchers have explored the effects of He on HEAs, including the formation of He bubbles, swelling, and irradiation hardening effect [40, 97, 98]. Comparisons between HEAs and traditional structural materials with similar FCC crystal structures have shown that HEAs experience lower void swelling due to He bubble formation. This could be attributed to the low mobility of He atoms and point defects in HEAs as well as the localized lattice distortion, potentially contributing to the higher He irradiation resistance of HEAs. Additionally, the He injection amount (He/dpa ratio) can significantly affect the size and density of secondary defects, such as bubbles and dislocations, which leads to the change in the void swelling behavior [99].

In this study, FCC Co-free $Cr_{0.8}$FeMnNi alloys and 316L were irradiated with Fe^{2+} at a temperature of 500℃ with different He^{+} pre-injection amounts. Transmission electron microscopy (TEM) observation was used to characterize the irradiation-induced defects to investigate the He injection amount effect on the microstructure evolution.

4.2 Experimental

The chemical composition of the base metal, including $Cr_{0.8}$FeMnNi and 316L, is presented in Table 1. The fabricating process of $Cr_{0.8}$FeMnNi has been described in section 3.2. 316L plate was supplied by Nippon Yakin Kogyo., LTD, Kawasaki Plant. The small piece of 316L was annealed at 1000 ℃ for 0.5 hours to eliminate the dislocation in the matrix. The composition of the materials was determined using X-ray

Fluorescence Spectroscopy (XRF) method (XRF, JEOL ／ JSX-3100RII).

Table 4.1 Chemical composition of $Cr_{0.8}FeMnNi$ and 316L base metals measured by XRF (at. %).

Materials	Cr	Fe	Ni	Mo	Mn
$Cr_{0.8}FeMnNi$	20.8	26.5	26.3	/	26.4
316L	17.6	Bal.	12.1	2.1	1.1

The fabricated samples were cut into φ3 mm disks, ground using SiC paper, followed by mechanical polishing (#2000) to the thickness of 100-150 μm. Then, the twin-jet electropolishing was conducted for irradiation experiments and characterization by TEM. The selected chemical for electropolishing was a mixture comprising 95% CH_3OH and 5% $HClO_4$. The electropolishing temperature was maintained from 5°C to 10°C, and the applied voltage was set to 30 V. The pre-injection of He^+ with a kinetic energy of 40 kV and 80 kV was performed at room temperature under vacuum condition 10^{-4} Pa using the ion accelerator attached with a Multi-beam High-Voltage Electron Microscope (HVEM) at Hokkaido University. The pre injection order is 80 kV first and then 40 kV to avoid the post-injection affect pre-injection regions. This process aimed to generate a uniform distribution of He atoms in the thin foil region. The SRIM calculation indicates He atoms are evenly-distributed at the depth of 150-200 nm as shown in Fig 4.1(a)-(c). The irradiation fluence for each He injection amount is shown in Table 2. The total He-injection amounts were 0, 1, 10, and 88 appm, respectively. Subsequently, heavy ion irradiation was conducted by using the High Fluence Irradiation Facility at the University of Tokyo (HIT) [100]. The samples were irradiated to a dose of 0.1 dpa(1.13×10^{14} ions/cm^2) by Fe^{2+}(1.0 MeV) at 500 ℃ using Gatan 652 double-tilt heating holder in a vacuum of 10^{-4} Pa. The specimen temperature is controlled using a bulk furnace and a water-cooled circuit. Fig 4.1 (d) shows that the irradiation dose at 170 nm reached 0.1 dpa. The irradiation fluence for each He injection amount is shown in Table 2.

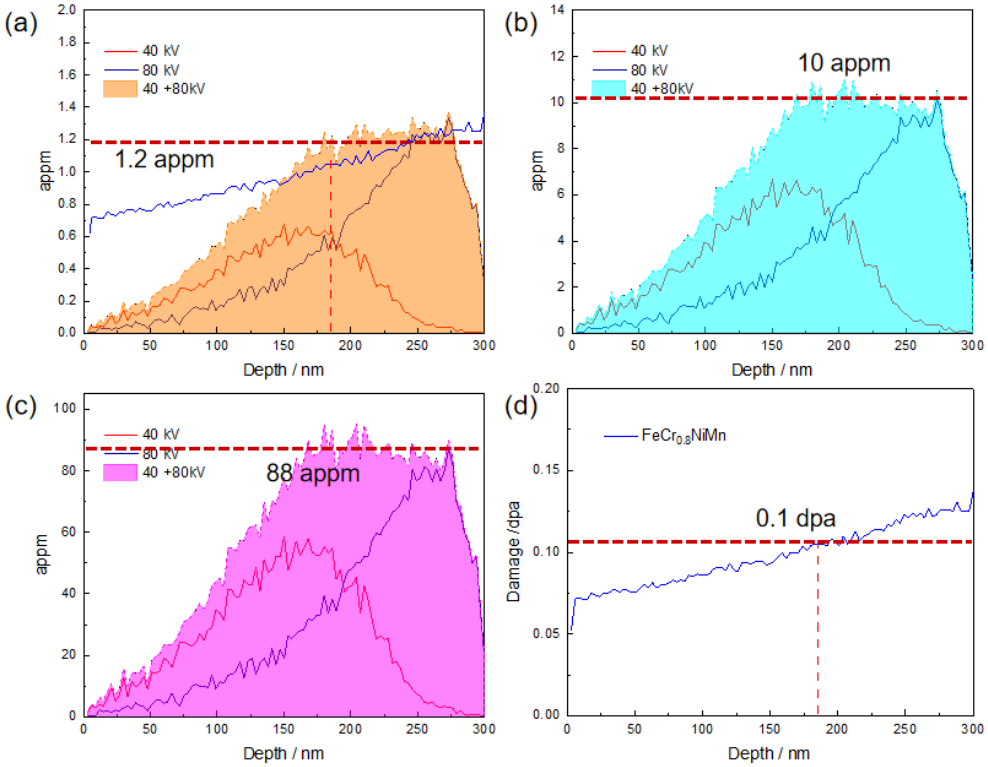

Fig 4.1 Depth profile of injected He atoms distribution at (a) 1 appm, (b) 10 appm, (c) 88 appm by 40 keV and 80 keV He^{+} irradiation and (d) displacement damage by 1.0 MeV Fe^{2+} irradiation

Table 4.2 Irradiation fluence for each He injection amount

He injected energy /kV	Ion fluence / ions·cm^{-2}		
	1 appm	10 appm	88 appm
40	0.773×10^{12}	0.77×10^{13}	0.673×10^{14}
80	1.95×10^{12}	1.48×10^{13}	1.48×10^{13}

During Fe^{2+} irradiation, in-situ observation was carried in TEM facility (JEOL JEM 2000EX) operated at 200kV. Further characterization of the microstructure was performed using TEM(JEOL JEM-2010) at Hokkaido University. This enabled the detailed observation of irradiation-induced defects, including the formation of black dots.

4.3 Results and discussion

4.3.1 The microstructure of $Cr_{0.8}FeMnNi$ and 316L after irradiation at 500℃

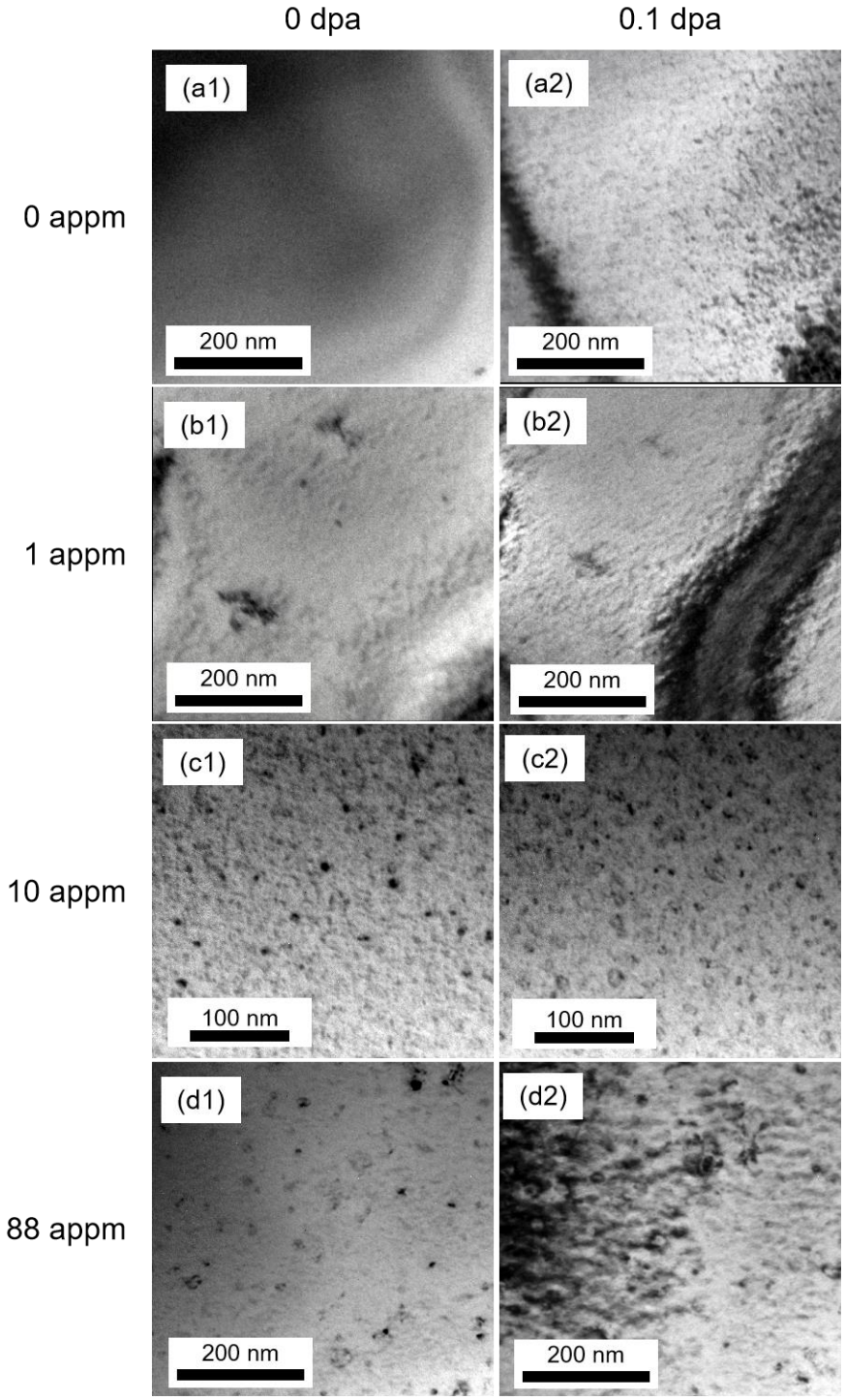

Fig 4.2 Bright field images of $Cr_{0.8}FeMnNi$ with He injection amounts of (a) 0 appm, (b)1 appm, (c) 10 appm, and (d) 88 appm at 0 and 0.1 dpa.

The microstructure evolution process was recorded during in-situ irradiation. Fig 4.2 shows the bright field images of $Cr_{0.8}$FeMnNi before irradiation(0 dpa) and at the end of irradiation(0.1 dpa). As shown in 4.2(a1)-(d1), some defects were generated in He injected samples as temperature reached 500 ℃ The He injected into the samples formed into small defects as temperature increased. At the beginning of irradiation, some irradiation induced defects, which are black dots in this work, generated and disappeared rapidly, which might be due to the surface effect and the recombination of interstitial atoms and vacancies at high temperature. As irradiation went on, some black dots formed, as shown in Fig 4.2(a2)-(d2). In 0 and 1 appm He injected samples, the black dots were relatively small in size, while in 10 and 88 appm He injected samples, larger black dots and some dislocation loops formed.

As shown in 4.3(a1)-(d1), contrary to $Cr_{0.8}$FeMnNi, no obvious defects were generated in 316L as temperature reached 500 ℃ The He injected into the samples formed into small defects as temperature increased. At the beginning of irradiation, some irradiation induced defects generated and disappeared rapidly, and black dots formed as irradiation went on, as illustrated in Fig 4.2(a2) -(d2). The evolution process of irradiation induce defects is similar to that of $Cr_{0.8}$FeMnNi.

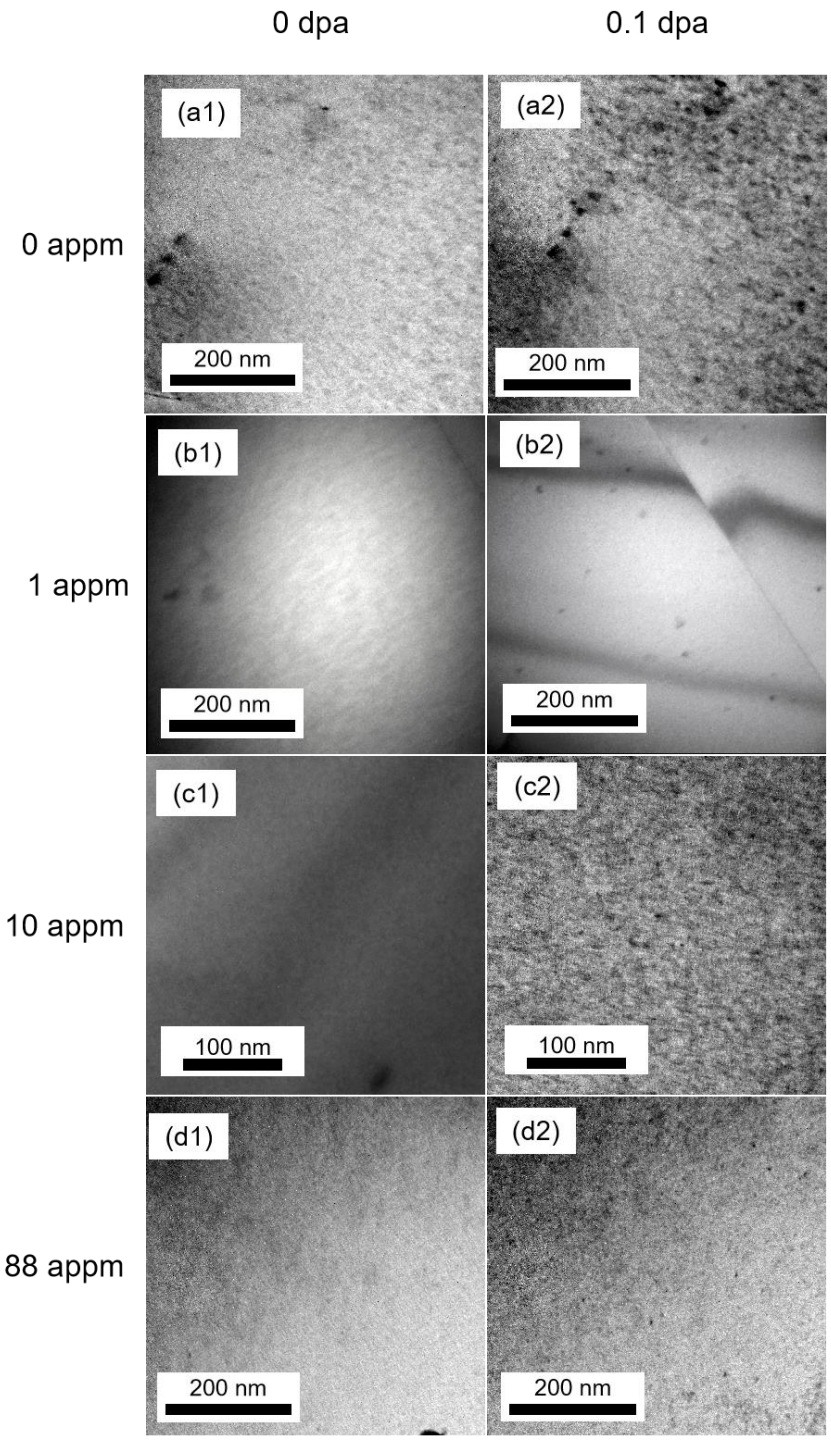

Fig 4.3 Bright field images of 316L with He injection amounts of (a) 0 appm, (b)1 appm, (c) 10 appm, and (d) 88 appm at 0 and 0.1 dpa.

After in-situ irradiation, TEM was used to further investigate irradiation induced defects. In MEAs, extra spots were generally found in diffraction patterns. Take $Cr_{0.8}FeMnNi$ with no He injection as an example, the bright field (BF) images and corresponding dark field (DF) images are shown in Fig 4.4. Some black dashes and

black dots, which might be irradiation defects can be found in the BF image, while only some small dots were found in the DF image of g=[200]. Therefore, the large dark contrasts with short dash and disk-shape represent the defects or oxide layer with extra spots. As illustrated in Fig 4.4(d), some stripes indicated by yellow circles are observed in the DF field of extra spots, indicating that some amorphous structure(which might be the oxide layer) formed after irradiation. The indexing of electron patterns results showed that all the extra spots are MnO oxide, which forms under low oxide condition.

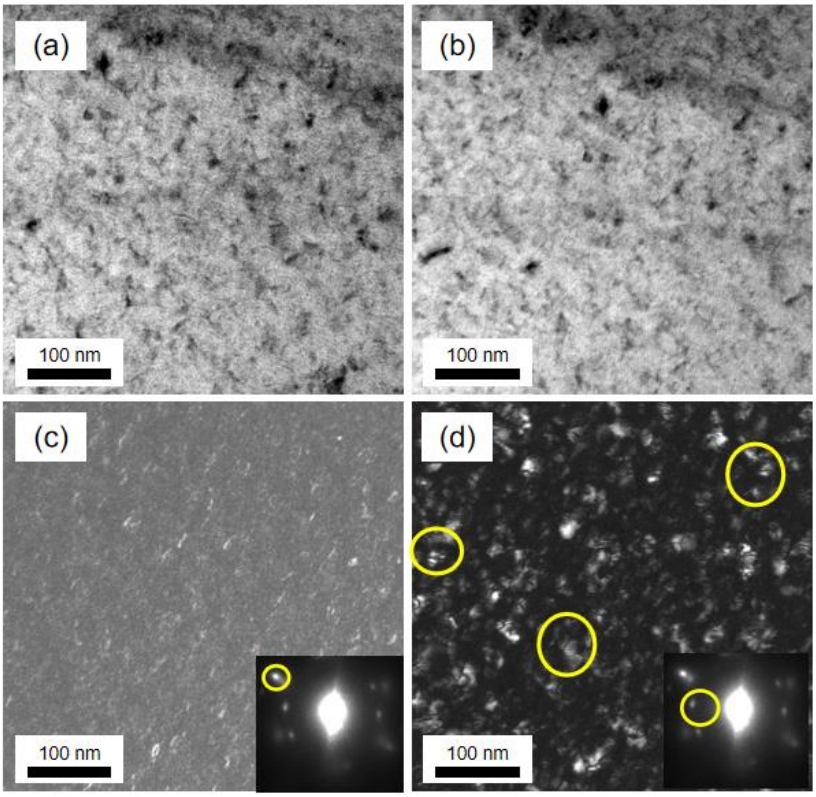

Fig 4.4 (a) and (b): BF images of $Cr_{0.8}$FeMnNi with no He injection; (c) DF image with g=[200], (d) DF image of the extra spots.

Fig 4.5 shows the BF and DF images with g=[111] in the matrix and near the grain boundary. The red circle indicates some amorphous structure (MnO). As He injection rate increased to 88 appm, the black dots in the matrix grew up and some small dislocation loops were found near the grain boundaries.

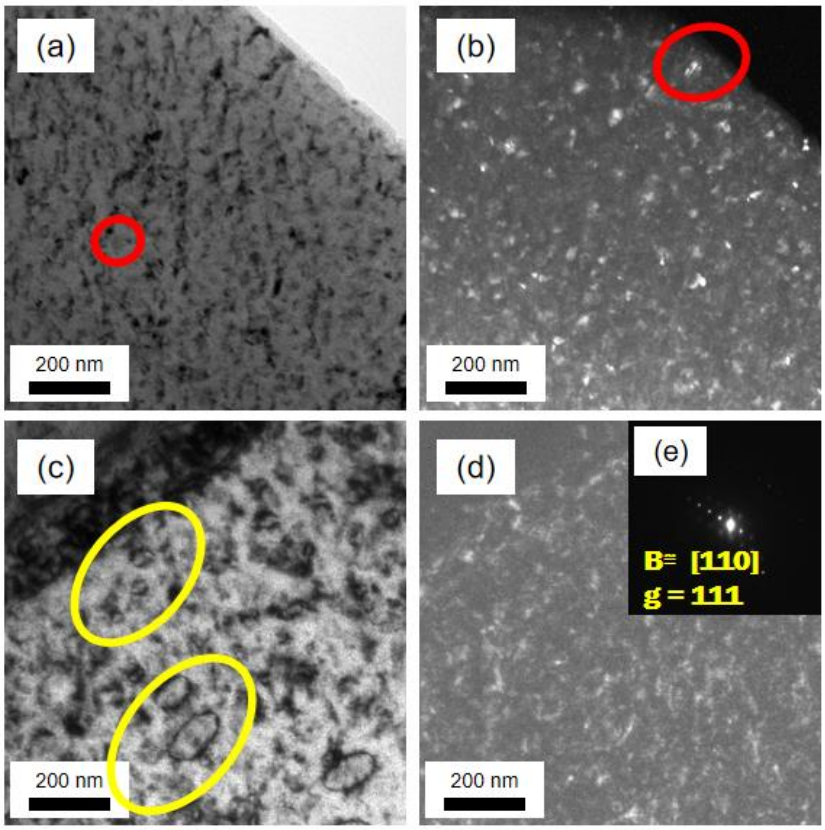

Fig 4.5 (a) and (b) BF and DF images of $Cr_{0.8}FeMnNi$ with 88 He injection; (c) and (d) BF and DF images near the grain boundary.

Fig 4.6 shows the microstructure with g=[111] of $Cr_{0.8}FeMnNi$ with different He injection amounts. (a)-(d) are the BF field images, and (e) -(f) are the corresponding DF images. The TEM analysis indicated no observable cavities in $Cr_{0.8}FeMnNi$, but it revealed irradiation-induced secondary defects and a surface oxide layer (shown in Fig. 4.6 (e)-(f)) in the samples irradiated at 500 ℃. The SAED pattern reveals that the oxide layer consists of MnO. Predominantly, the irradiation resulted in the formation of black dots, with the average size of these dots appearing to increase with the He injection amount. During the statistical process, weak beam dark field images were captured.

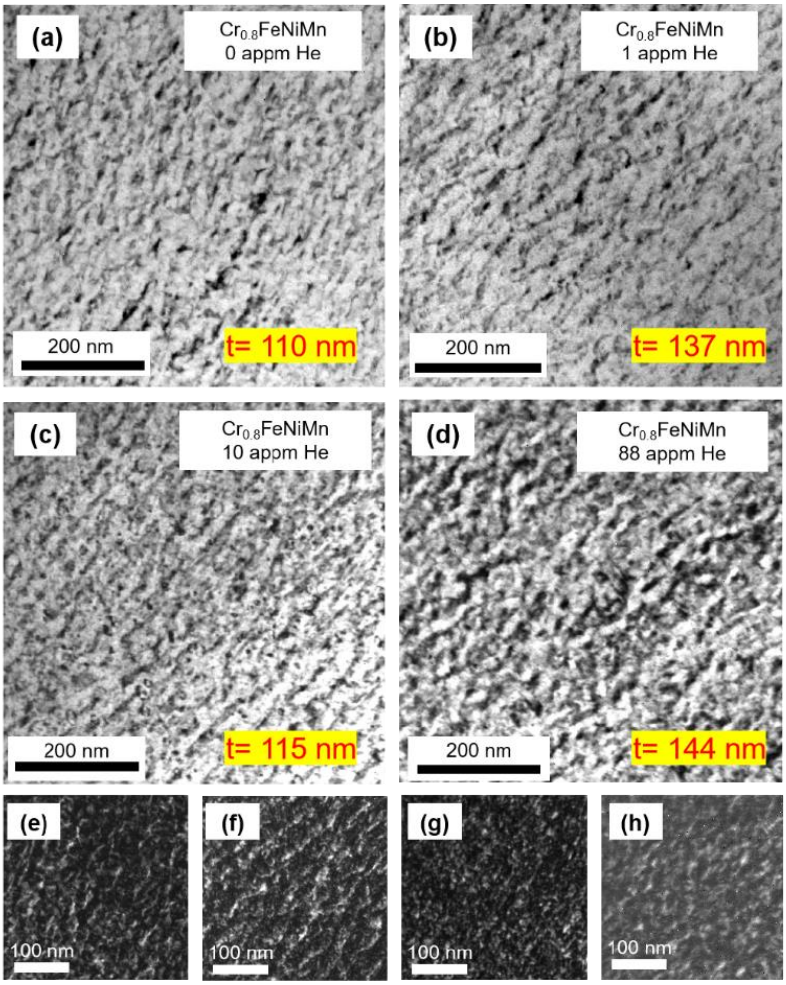

Fig 4.6 Microstructure of the $Cr_{0.8}FeMnNi$ MEA injected with different He fluence and then irradiated with Fe^{2+} at 500℃. (a) 0 appm He, (b) 1 appm He, (c) 10 appm He, (d) 88 appm He, (e)-(f) the corresponding WBDF images of (a)-(d) showing the oxide layer.

To mitigate the influence of the oxide layer, the diffraction spots corresponding to the oxide layer were selected with the objective aperture at the same position, and then dark field images were captured. By comparing the dark field images of defects and the oxide layer, the oxide layer was excluded, and the number and size of black spots were counted. Additionally, the convergent-beam electron diffraction (CBED)[101] method was employed to ascertain the thickness at the observation sites, with the thickness of all observation regions falling in the range of 110~206nm.

The analysis of convergent-beam electron diffraction patterns for foil thickness is easily carried out in the two-beam approximation to dynamical diffraction theory. Fig 4.7 shows the selection of typical two-beam dynamic conditions patterns taken from $Cr_{0.8}FeMnNi$ with 88 appm He injection amount using a (111) reflection. The values of

S_i, are determined by measuring the distance $\Delta\theta_i$ from the center of the diffracted beam profile to each of the successive minima, together with the distance $2\theta_d$ between the center spot and the diffracted spot. The value of $2\theta_d$ can be obtained by measuring the distance between corresponding positions on the image of the condenser aperture that defines each spot. The details are shown in Table 4.3.

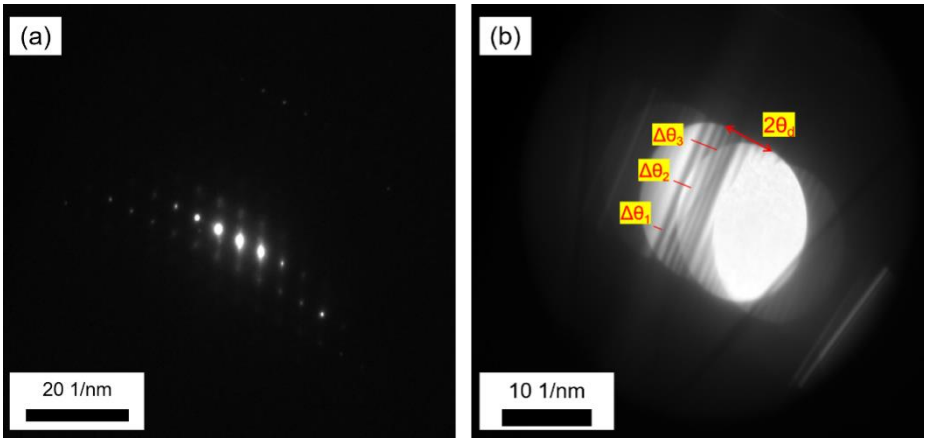

Fig 4.7 (a)Two-beam (111) diffraction pattern, and (b) the convergent beam diffraction patterns of $Cr_{0.8}FeMnNi$ with 88 appm He injection amount.

The thickness t of the foil sample could be obtained by measuring $\Delta\theta_i$ and $2\theta_d$ measurements via the equation,

$$S_i = \frac{\lambda}{d^2}\left(\frac{\Delta\theta_i}{2\theta_d}\right) \quad (4\text{-}1)$$

where λ is the wavelength and d is the spacing of the operating reflection. In this research, the voltage of TEM was 200 kV, thus λ can be derived as 0.00273nm. d is the spacing of the (111), which is 0.2384nm in this work.

Table 4.3 Parameters of foil thickness calculation using CBED method in 88 appm He injected $Cr_{0.8}FeMnNi$.

Parameters	S_1	S_2	S_3
$\Delta\theta_i$ / nm^{-1}	0.488	1.465	2.305
S_i / nm^{-1}	0.00559	0.01674	0.02640

The analysis of CBED patterns for foil thickness values is best accomplished by a regression analysis of the appropriate equations of the two-beam approximation to dynamical diffraction theory (not including absorption). As shown in Fig 4.8, the relationship between $(S_i/n_i)^2$ and $(1/n_i)^2$ is ascribed to the following equation,

$$\left(\frac{S_i}{n_i}\right)^2 + \left(\frac{1}{n_i^2}\right)\left(\frac{1}{\xi_g^2}\right) = \frac{1}{t^2} \quad (4\text{-}2)$$

where ξ_g is known to sufficient accuracy. Regression analysis of the positions of intensity minima and maxima thus allows both t, and ξ_g to be determined. The foil thickness of 88 appm He injected $Cr_{0.8}FeMnNi$ is 137 nm.

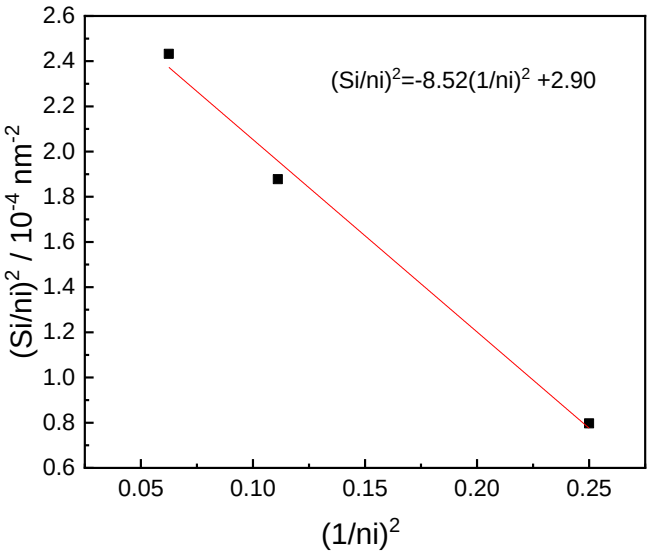

Fig 4.8 The linear relationship between $(S_i/n_i)^2$ and $(1/n_i)^2$

Fig 4.9 shows the bright field images of 316L. No observable cavities and discernible oxide layer were found, but irradiation-induced black dots were indeed observed in the irradiated 316L. Furthermore, both the average size and the number density of the black dots seemed to decrease in the 1 appm He-injected sample(10 appm He/dpa). Meanwhile, the average size decreased as He injection amount increased, which is the opposite trend with irradiated $Cr_{0.8}$FeMnNi.

The thickness of $Cr_{0.8}$FeMnNi ranges from 110-137 nm and the thickness of 316L in He-injected samples varies from 137-144 nm as Fig 4.9 showed. The thickness of the observation area for each alloy is similar. Therefore, surface effect difference in each alloy is relatively small. The changing trend of defect size and density is the main comparison factor, so although the thickness of the two materials are different, the trend comparison is reliable. Subsequently, statistical calculations were conducted to determine the average size and number density of the black dots.

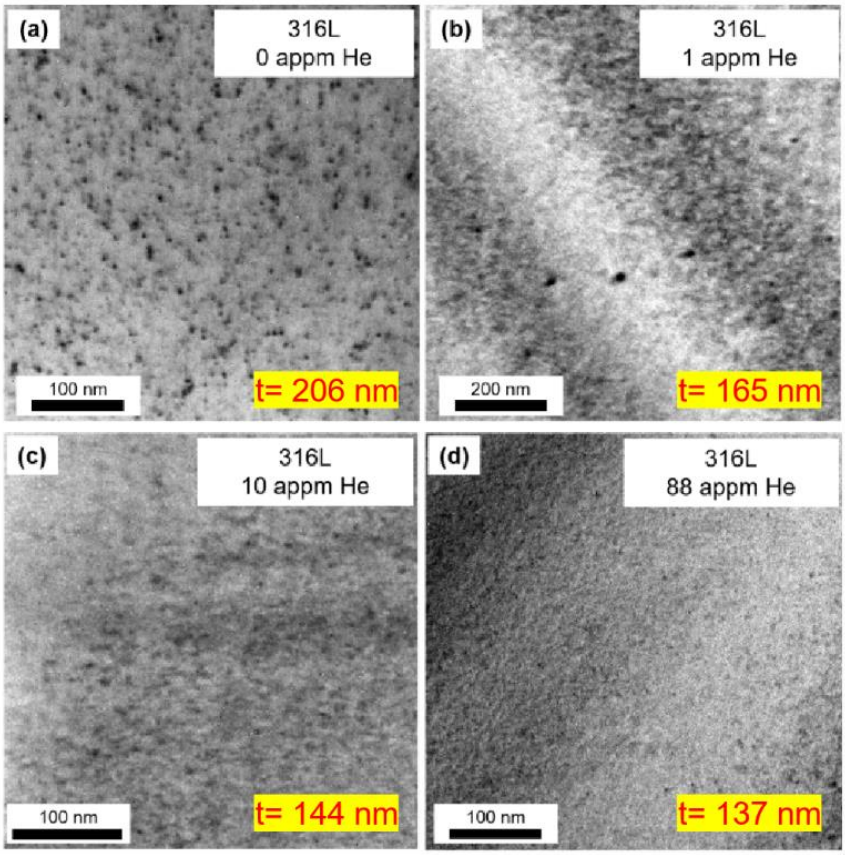

Fig 4.9 Microstructure of the 316L injected with different He fluence and then irradiated with Fe^{2+} at 500℃. (a) 0 appm He, (b) 1 appm He, (c) 10 appm He, (d) 88 appm He.

4.3.2 The size and number density of defects in $Cr_{0.8}FeMnNi$ and 316L

Fig 4.10(a) illustrates the size distribution of the defects observed in $Cr_{0.8}FeMnNi$. In $Cr_{0.8}FeMnNi$ samples, the size range of the black dots changed from 2-12 nm in the sample without He injection to 3-14 in the samples with 88 appm He (880 appm He/dpa). In the sample without He-injection, the size peak was at 5 nm, with small black dots (≤ 5 nm) comprising over 50% of the total defects. As the He injection amount increased, both the peak size and the proportion of the large size defects increased. In the sample with 88 appm He injection, the peak size was 7 nm and the proportion of large black dots (> 7 nm) was larger compared with the sample without He injection.

The size distribution of black dots in 316L is shown in Fig 4.10(b). The size range of black dots in the sample without He injection spanned from 3 nm to 13 nm while in the sample with 88 appm He injection, the size ranged from 2 nm to 10 nm. The peak

size showed a contrasting trend from $Cr_{0.8}FeMnNi$. The peak size in no He-injected sample was 8 nm and the proportion of small defects is about 60%, while the peak size in the sample with 88 appm He injection shifted to 4 nm.

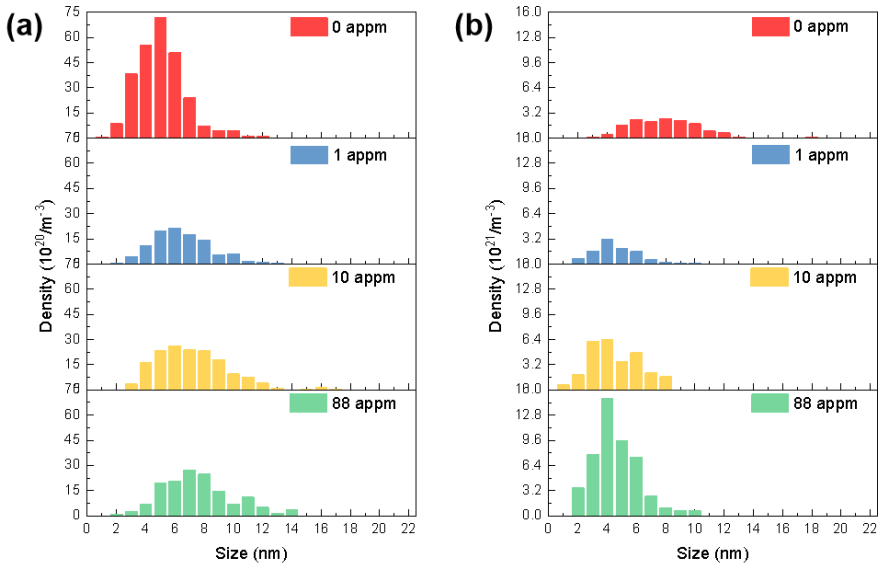

Fig 4.10 Size distribution of the black dots in (a) $Cr_{0.8}FeMnNi$ and (b) 316L.

The average size and number density of black dots of $Cr_{0.8}FeMnNi$ and 316L are shown in Fig 4.11. In no He-injected samples, the black dots in $Cr_{0.8}FeMnNi$ exhibited smaller size and higher number density compared to those in 316L. As He concentration increased to 1 appm, the density of black dots decreased in both $Cr_{0.8}FeMnNi$ and 316L. However, while the size of black dots in $Cr_{0.8}FeMnNi$ increased, 316L exhibited a different trend. With further increases in He concentration, the size and number density of black dots increased slightly in $Cr_{0.8}FeMnNi$. However, in 316L samples, the number density increased significantly while the average size decreased slightly. Notably, the increase in number density in $Cr_{0.8}FeMnNi$ trend was less than that in 316L. Meanwhile, although the number density of black dots in $Cr_{0.8}FeMnNi$ and 316L are in the same order of magnitude, the oxide layer observed in $Cr_{0.8}FeMnNi$ samples has little effect on the surface sink.

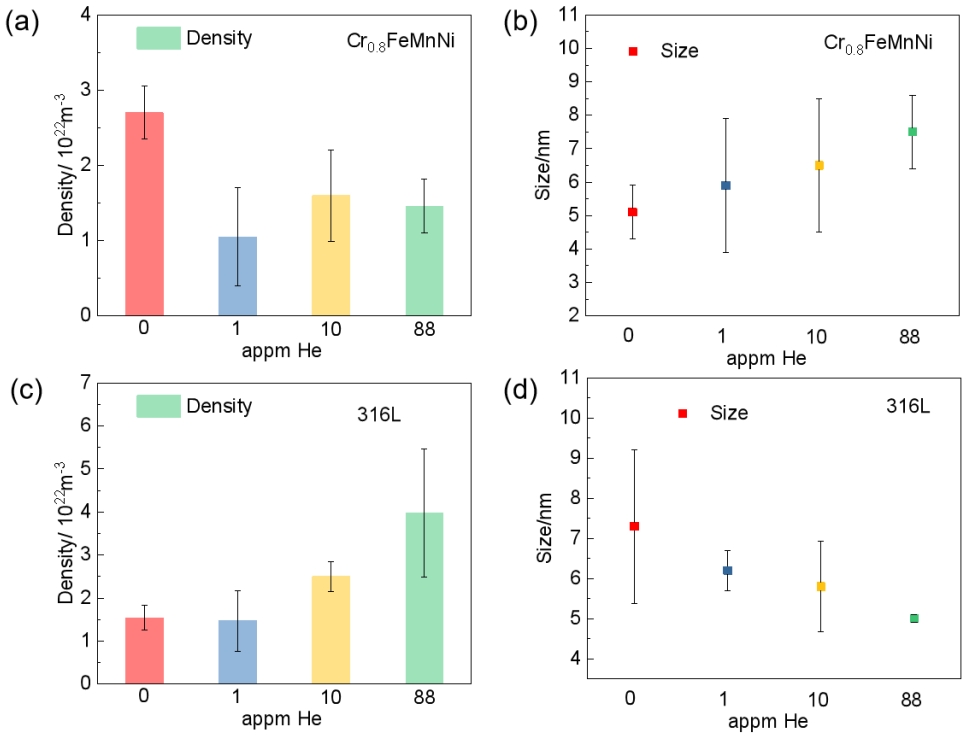

Fig 4.11 The number density(a), (c) and average size (b), (d) of the defects in $Cr_{0.8}$FeMnNi and 316L.

4.3.3 He injection amount effect on the evolution of $Cr_{0.8}$FeMnNi and 316L

During irradiation, atoms are knocked out from their original lattice positions, producing a large number of point defects, such as vacancies and self-interstitial atoms (SIA). Displacement damage initiates complex microstructural evolution, characterized by the accumulation of vacancy and SIA clusters, changes in the dislocation structures, and the formation of voids. Furthermore, displacement damage also interacts complexly with the transmutation product, He atoms [44]. The behavior of He atoms is also affected by vacancies and SIAs induced by radiation [102].

In the irradiation process where He atoms are introduced along with displacement damage, He atoms tend to form helium-vacancy (He-V) complex with radiation-induced and thermal vacancies, and interstitial atoms and He atoms compete to react with vacancies [103]. Meanwhile, the presence of high-concentration SIAs generated by irradiation may affect the nucleation of He bubbles and the evolution of defects. Some researchers have investigated the binding energy of SIAs to He-V cluster using

molecular dynamics (MD) simulations [102], showing that the binding energy of SIAs to He-V cluster in tungsten (W) decreases from 12.0 eV to 2.0 eV when the He-to-vacancy ratio is increased from 0 to 8. In such cases, He-V clusters tend to combine with SIAs in the matrix.

In cases where the He-to-vacancy ratio of the He-V cluster is larger than 3, the binding energy of vacancies to He-V clusters is much higher than the binding energy of SIAs to He-V complexes. In such cases, He–vacancy clusters tend to combine with another vacancy and expel an SIA to the surface. Moreover, when He–to-vacancy ratio exceeds 6.8 in the He-V cluster, He-V clusters are more readily combined with He atoms compared to the SIAs W [102]. A similar phenomenon, where the binding energy of SIAs to He-V clusters decreases with increasing He-to-vacancy ratio, was also found in nickel and palladium [104]. In this study, since all samples were irradiated to the same dose, it is presumed that the number of vacancies induced by collision cascade remained consistent. Thus, a higher He concentration corresponds to a higher He-to-vacancy ratio and diminished binding energy of SIAs to the He-V complex.

In this study, as illustrated in Fig 4.11, the black dots in $Cr_{0.8}$FeMnNi without He injection exhibited smaller size and higher number density than those in 316L samples. According to the previous studies, In HEAs, alloying TMs with large differences in valence electron counts may lead to chemical disorder, resulting in much shortened mean free path as well as the reduction in both electrical and thermal conductivity. Therefore, the energy dissipation in HEAs is slower than traditional alloys, contributing to more localized heat and longer and greater temperature rises, which might enhance the recombination of point defects[105]. The high local lattice distortion enlarge the local atomic-level pressure, which can further impact the defect formation energies and migration behaviors and further promote the defects recombination[105-107]. Compared with 316L, the high recombination of point defects in $Cr_{0.8}$FeMnNi reduce the defect production. Therefore, the black dots in $Cr_{0.8}$FeMnNi have smaller size and higher number density than those of 316L samples.

As shown in Fig 4.12(a), interstitial atoms and vacancies induced by collision cascade during the irradiation process have the propensity to migrate and form SIA clusters and vacancy clusters, or recombine with each other. However, in the 1 appm He-injected samples, He atoms tend to coalesce with radiation-induced as well as thermal vacancies, forming stable He-V complexes. As illustrated in Fig. 7(b), under

low He amount conditions, both interstitial atoms and vacancies tend to combine with He-V complexes(as indicated by the red and black arrows). However, at low centration, due to the higher binding energy of SIAs to He-V clusters compared to that of vacancies, a large number of SIAs are bound to He-V clusters, resulting in a reduction in the number of interstitial atoms in the matrix compared to samples without He injection. This phenomenon contributes to a decrease in the number density of black dots. As the He amount increases, the number density of the black dots in both $Cr_{0.8}$FeMnNi and 316L increases. As discussed earlier, the binding energy of SIAs to He-V clusters diminishes with increasing He injection amount. Consequently, Fig. 7(c) illustrates that at higher He injection amount situation, He-V clusters tend to absorb more vacancies and expel more interstitial atoms. The more He injection amount, the more SIA will be kicked out. The accumulated SIAs within the matrix tend to aggregate and nucleate, increasing the number density of black dots as the He amount escalates.

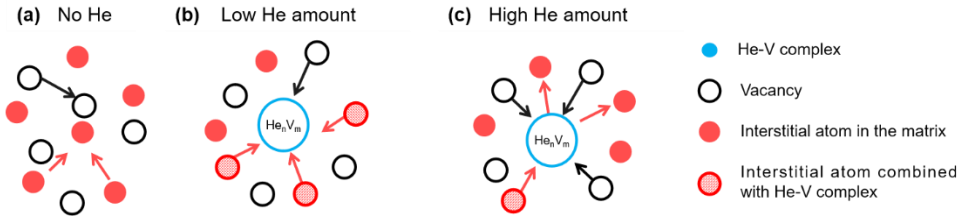

Fig 4.12 Schematic explanation of the interaction between SIA and vacancy with He-V complex at different He injection amount.

Furthermore, the size of black dots in $Cr_{0.8}$FeMnNi increase while the size of black dots decreased with He injection amount. From other researcher's work, the migration energy of interstitial atoms in $Cr_{0.8}$FeMnNi (0.19 eV) is much smaller than 316L(0.9 eV)[108]. The mobility of interstitial atoms in $Cr_{0.8}$FeMnNi is larger than in 316L. So the SIAs which were kicked out from the He-V complex due to the increase of He injection amount can migration for a long distance and combine with each other, resulting in the growth of black dots. However, He can inhibit the migration of point defects. As He injection increase, the migration of SIAs in 316L is suppressed. The SIAs kicked out from He-V complex tend to nucleate and form small black dots. Therefore, the average size of black dots in $Cr_{0.8}$FeMnNi and 316L show different trends and the increasing trend in number density of $Cr_{0.8}$FeMnNi is much smaller compared to 316L.

4.4 Summary

In this study, FCC Co-free MEA $Cr_{0.8}FeMnNi$ and 316L were irradiated with Fe^{2+} to the same dose but with different amounts of He injected to investigate the effect of He injection amount on microstructural evolution. The main conclusions are summarized as follows.

(1) In the absence of He injection, irradiation-induced black dots in $Cr_{0.8}FeMnNi$ exhibited with smaller size and higher number density compared to those in 316L. his can be attributed to the short-distance migration of point defects in $Cr_{0.8}FeMnNi$, which arise from the diversity in atomic radii, intricate local atomic environments, and complex interactions. These factors promote the recombination process of irradiation-induced defects, leading to the formation of small black dots with higher number density.

(2) The binding energy of self-interstitial atoms (SIA) to He-V complexes decreased with increasing He injection rate. In $Cr_{0.8}FeMnNi$ with low He amount, interstitial atoms tend to combine with He-V complexes, leading to the decrease in the number density of black dots. However, as the He amount increased, the binding energy between interstitial atoms and He-V complexes decreased. Consequently, a large number of SIAs could be expelled into the matrix, enhancing the nucleation of black dots. Thus, the number density of black dots increased with increasing He amount.

(3) The promoted recombination of point defects result in the small size and high density of black dots in $Cr_{0.8}FeMnNi$. The small interstitial migration energy in $Cr_{0.8}FeMnNi$ compared with 316L result in the different size trend as He injection amount increase.

Chapter 5

He and H effect on swelling behavior and mechanical properties in ion-irradiated MEAs

5.1 Introduction

As one of the decisive factors for the safe and efficient operation of nuclear reactors, structural materials have been identified as an important component in developing nuclear power [109, 110]. The stringent working environment in the next-generation fission/future fusion nuclear reactors poses a major challenge to the design of structural materials [111]. The displacement cascades produce vacancies, interstitials, and a variety of extended defects, but of particular concern is the simultaneous production of helium and hydrogen at dose rates and accumulated concentrations for which the materials and engineering communities have little practical experience and hence, little understanding. Both H and He have a strong impact on the microstructure evolution of irradiated materials. Typically, they may cause additional swelling and embrittlement of materials. Lots of research has been done to clarify the effect of H [112-119] and He[120-126] on the irradiation related damage in structural materials.

Ion irradiation is gaining interest as a surrogate for neutron irradiation because it is fast, cheap, and effective [127-129]. However, ion irradiation does not include the effects of transmutation that produces gasses such as helium and hydrogen, necessitating pre-implantation or co-injection, which has been shown to enhance cavity nucleation across many alloy systems.

The study in section 4 was performed with pre-implanted helium. However, the damage level is too low to draw any meaningful conclusions about the effect of helium on cavity growth and subsequent swelling. Although the study demonstrates that the addition of helium can affect the nucleation and growth of black dots, the effect of helium on cavity growth and swelling at high damage levels with co-injected helium remains unclear.

Therefore, this work seeks to provide a clear understanding of the effect of coinjected helium and hydrogen on MEAs to high damage levels at high temperature. $Cr_{0.8}$FeMnNi and 316L are irradiated with single beam (Fe^{3+}), dual beam (Fe^{3+}+He^{+}), and triple beam (Fe^{3+}+He^{+}+H^{+}) at 500℃. Nanoindentation and TEM are used to characterize the hardness increment and microstructure evolution to investigate the irradiation behavior and the helium and hydrogen effect on MEAs.

5.2 Experimental

Four Cr-Fe-Mn-Ni MEAs $Cr_{0.65}FeMnNi$, $Cr_{0.8}FeMnNi$, $Cr_{0.8}FeMn_{1.3}Ni$, $Cr_{0.8}FeMn_{1.3}Ni_{1.3}$ were fabricated by argon (Ar) gas protected arc-melting method. Subsequently, the as-cast alloys were homogenized at 1100 ◦C for 48 hours. Then, the samples were cold-rolled to reduce the total thickness by 80%, followed by recrystallization at 1000 °C for 4 hours. All the heat-treatments were conducted by individually encapsulated samples in evacuated quartz tubes.

The bulk material prepared by the method described before was cut into plates with the size of 6 mm × 3 mm × 0.5 mm, as shown in Fig 5.1. The irradiated surface was grounded using SiC paper, followed by mechanical polishing (#2000 and diamond spray of 1 μm). Ion irradiation experiments were performed at Takasaki Ion Accelerators for Advanced Radiation Application(TIARA) using single, dual, and triple beam irradiation. The irradiation conditions are shown in Table 5.1. In this irradiation experiment, a 0.8 μm thick Al foil was used as an energy degrader for He^+ and H^+, and the distribution was adjusted to have a width in the depth direction. The irradiated region is in the center of the sample, while the unirradiated regions are on both sides of it. After irradiation, the samples were scratched around the boundary of the irradiated and unirradiated regions as a mark for further observation.

Table 5.1 Irradiation condition.

	Ions	Energy / MeV	rate	Temperature / 500 ℃	dpa at 1 μm	Materials
Single	Fe^{3+}	10.5	/	500 ℃	18.4	$Cr_{0.65}FeMnNi$ $Cr_{0.8}FeMnNi$ $Cr_{0.8}FeMnNi_{1.3}$ 316L
Dual	Fe^{3+}	10.5	/		21.1	$Cr_{0.65}FeMnNi$ $Cr_{0.8}FeMnNi$ $Cr_{0.8}FeMnNi_{1.3}$ 316L
	He^+	1.05	15 appm He/dpa			
Triple	Fe^{3+}	10.5	/		23.7	$Cr_{0.65}FeMnNi$ $Cr_{0.8}FeMnNi$ 316L
	He^+	1.05	15 appm He/dpa			
	H^+	0.38	40 appm H/dpa			

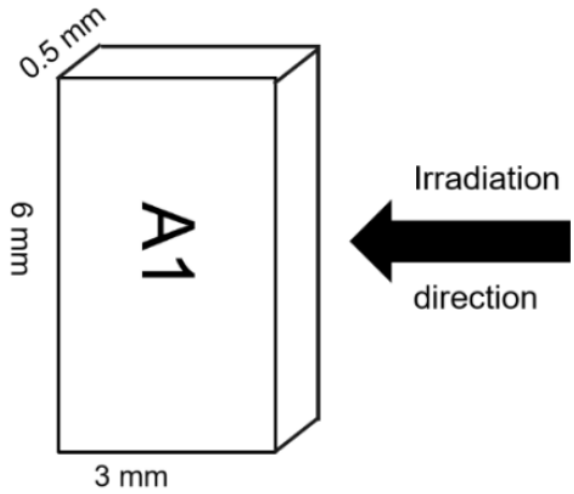

Fig 5.1 Schematic diagram of the specimen for ion irradiation.

The typical depth profile of the displacement damage and He and H distribution was calculated by the SRIM as Fig 5.2. The area near the surface strongly has the effect of surface sink, and the damage peak region has a large dpa gradient. He/dpa ratio and H/dpa ratio at the depth of 1 μm varies slightly, and the absolute value is 15 appm He/dpa and 40 appm H/dpa, respectively.

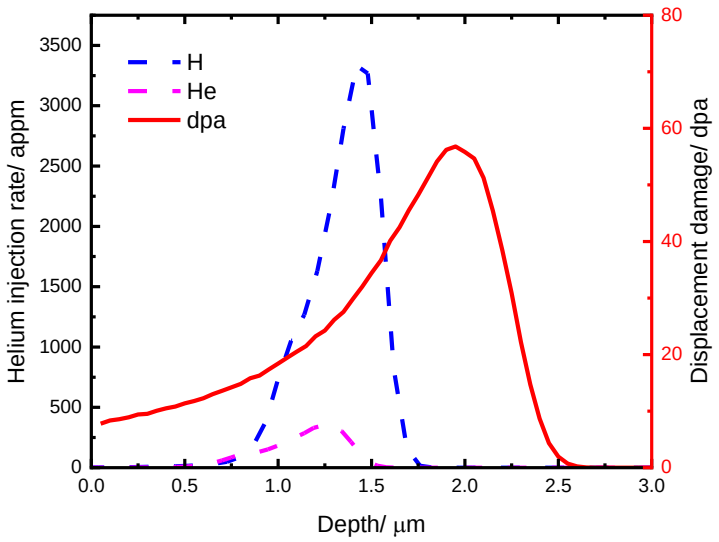

Fig 5.2 Depth profile of displacement damage (dpa) and atoms distribution.

To investigate the irradiation hardening, nano-indentation experiments were conducted on both irradiated and unirradiated areas of the samples. Nano-indenter (Hysitron TI-950) for single indentation at a constant indentation depth of 300 nm. At least 9 typical indents were conducted on each area with a distance of 15 μm which was

larger than five times the largest indentation diameter so that the hardness will not be affected by other indents.

The irradiated sample was picked up into a strip using a FIB (Hitachi, FB-2100), and then thinned into a thin film which has a thickness of about 100-180 nm using an FIB (JEOL, JIB-4601F). The specimen for TEM and STEM observation was extracted by focused ion beam (FIB, Hitachi FB2100; JEOL JIB-4601F) using 30kV Ga^+ for machining and 10kV Ga^+ for polishing.

5.3 Results and discussion

5.3.1 Irradiation induced hardening

Table 5.2 shows the nano-indentation hardness results of each alloy. The irradiation hardening results are illustrated in Fig 5.3. For single beam (Fe^{3+}) irradiated alloys, $Cr_{0.65}FeMnNi$ and $Cr_{0.8}FeMnNi$ showed relatively small hardness increment, while 316L showed the highest hardness increment value. In the dual beam ($Fe^{3+} + He^+$) irradiated alloys, irradiation induced hardening effect is larger than single beam irradiated samples. The harness increments of $Cr_{0.65}FeMnNi$ and $Cr_{0.8}FeMnNi$ are still low compared to the other two alloys, while $Cr_{0.8}FeMnNi_{1.3}$ and 316L still have high harness increment. However, for triple beam ($Fe^{3+} + He^+ + H^+$) irradiated alloys, the hardness result of irradiated region in $Cr_{0.65}FeMnNi$ and $Cr_{0.8}FeMnNi$ is smaller than unirradiated area. 316L still showed the largest hardening effect than MEAs.

Table 5.2 Irradiation induced hardening at the depth of 300 nm of MEAs and 316L.

Irradiation condition	Materials	Unirradiated region / GPa	Irradiated region / GPa	Irradiation hardening / GPa
Single	$Cr_{0.65}FeMnNi$	2.25±0.17	2.47±0.51	0.22
	$Cr_{0.8}FeMnNi$	2.76±0.11	2.86±0.49	0.10
	$Cr_{0.8}FeMnNi_{1.3}$	2.75±0.13	3.72±0.53	0.97
	316L	2.75±0.10	3.80±0.57	1.05
Dual	$Cr_{0.65}FeMnNi$	2.97±0.12	3.37±0.75	0.40
	$Cr_{0.8}FeMnNi$	2.93±0.32	3.29±0.69	0.36
	$Cr_{0.8}FeMnNi_{1.3}$	2.80±0.15	4.00±0.72	1.2
	316L	3.13±0.26	4.00±0.21	0.87
Triple	$Cr_{0.65}FeMnNi$	1.44±0.09	1.36±0.16	-0.08
	$Cr_{0.8}FeMnNi$	1.67±0.07	1.41±0.13	-0.26
	316L	2.44±0.21	3.86±0.18	1.42

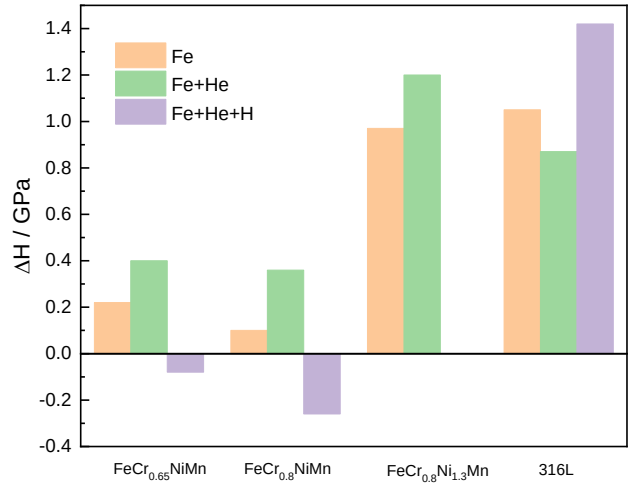

Fig 5.3 Irradiation induced hardening at the depth of 300 nm.

5.3.2 Microstructure after irradiation

It is well known that irradiation defects such as He bubbles and dislocations would be generated in structural materials after irradiation with He injection. Helium is thermodynamically insoluble in metals and tends to precipitate into bubbles if the temperature is high enough for the helium atoms to migrate, which results in high swelling in materials. According to some research, swelling may be enhanced due to helium generation, which may limit the lifetime of the current-generation materials [130].In this work, the voids and swelling at the depth of 1 μm with 15 appm He/dpa and 40 appm H/dpa were analyzed to investigate He and H effect on swelling of $Cr_{0.8}$FeMnNi and 316L.

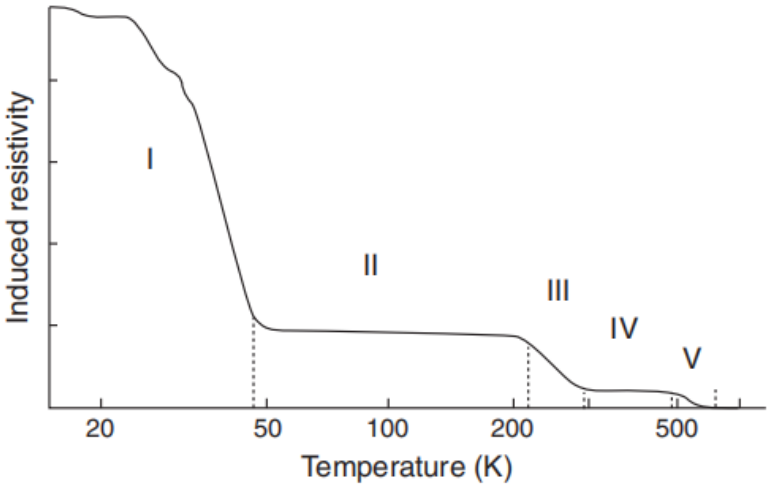

Fig 5.4 Electrical resistivity defect recovery stages for copper following electron irradiation at 4K.

Irradiation temperature typically invokes a very large influence on the

microstructural evolution of irradiated materials. There are several major temperature regimes delineated by the onset of migration of point defects. Fig. 5.4 shows the five major defect recovery stages for copper irradiated with electrons at 4K [131]. Stage I corresponds to the onset of long-range SIA migration. This stage always relates to the close-pair (correlated) recombination of Frenkel defects from the same displacement event and long range uncorrelated recombination of defects from different primary displacement events. Stage II involves the migration of small SIA clusters and SIA-impurity complexes. Stage III corresponds to the onset of vacancy motion. Stage IV involves the migration of vacancy–impurity clusters, and Stage V corresponds to the thermal dissociation of sessile vacancy clusters. Cavities and bubbles formed in stage IV, which might induce void swelling in this stage. The major microstructural difference from lower temperature irradiations in most materials is the emergence of significant levels of swelling. As temperature increases, swelling decreases due to due to enhanced thermal annealing of sessile vacancy clusters. The phenomenon that swelling increases first and decreases with increasing temperature can be found in various materials. As shown in Fig 5.5, the relationship of swelling of different materials with temperature is illustrated.

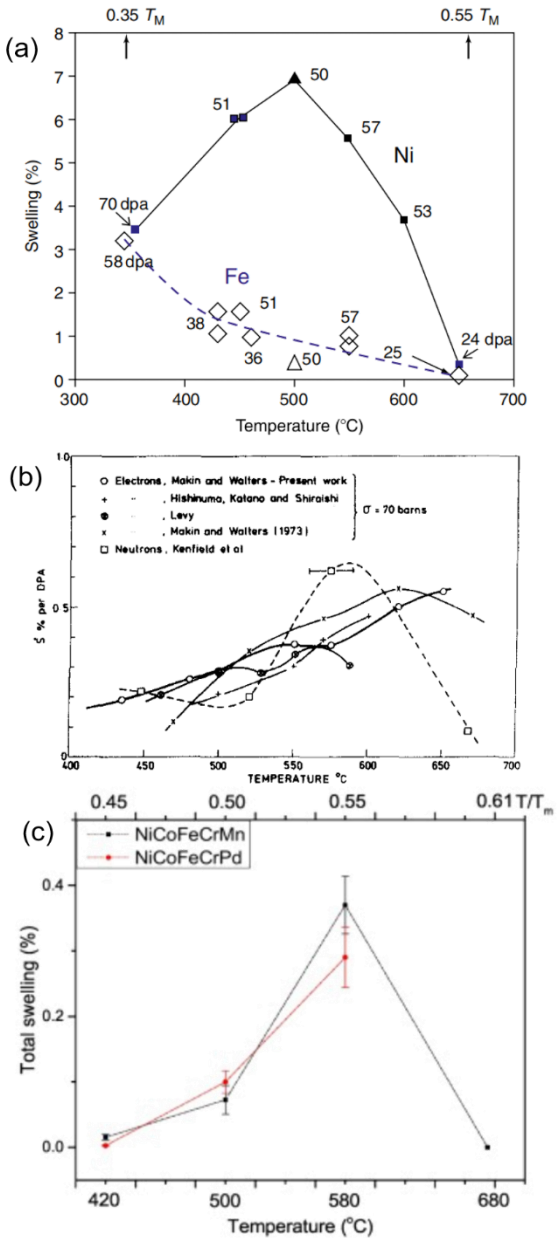

Fig 5.5 (a) Comparison of the temperature-dependent void swelling behavior in Fe and Ni [132]. (b) Comparison of the results by various authors on the temperature dependence of the swelling rate of ST316 steel during electron and neutron irradiation[133]. (c) Temperature dependence of overall swelling in Mn-HEA and Pd-HEA irradiated by 3.0 MeV Ni^{2+} ions to 5×10^{16} cm^{-2} [134].

To further explain the difference in irradiation hardening effect and swelling for each alloy under different irradiation condition, a detailed analysis of the microstructure of $Cr_{0.8}FeMnNi$ and 316L, which have the highest and lowest irradiation-induced hardening was conducted on TEM and STEM.

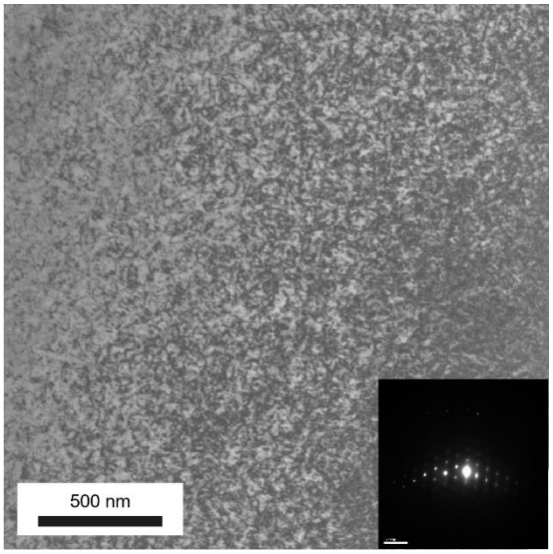

Fig 5.6 Bright field image of single beam irradiated $Cr_{0.8}FeMnNi$ with g=[200].

Basically, irradiation hardening is caused by precipitates, dislocation loops, Frank loops, cavities and He bubbles. However, in this work, due to the high displacement damage, the dislocation density is high and difficult to measure, as Fig 5.6 shows. Meanwhile, due to the relatively high irradiation temperature, no Frank loop was found in these samples. Thus, the microstructure characterization focuses on the cavities and bubbles.

Fig 5.7 illustrates the microstructure at different depths of single beam irradiated $Cr_{0.8}FeMnNi$. From Fig 5.7(b), due to the surface effect, no obvious cavity was found, while some particles that have an average size of 100 nm were found at the surface. When foil samples are thin enough, free surface effects are expected [135]. These generally include trapping of point defects at the surfaces of the foil resulting in depleted areas along these surfaces. As a result, the thin edges of our in-situ implanted specimens are free of bubbles in contrast with thicker regions. STEM-EDX method was used to check the element distribution near the surface. As Fig 5.8 shows, the particles are composed of Cr, Mn, and O. Cavities were found in single beam irradiated $Cr_{0.8}FeMnNi$. The distribution of cavities can be divided into some parts according to the properties of cavity size and density. From 0.1-1.5 μm, some cavities formed and the size increased with increasing dose as shown in Fig 5.7(d). However, the size of cavities decreased as damage kept increasing and the size increased at the depth of 2.3 μm.

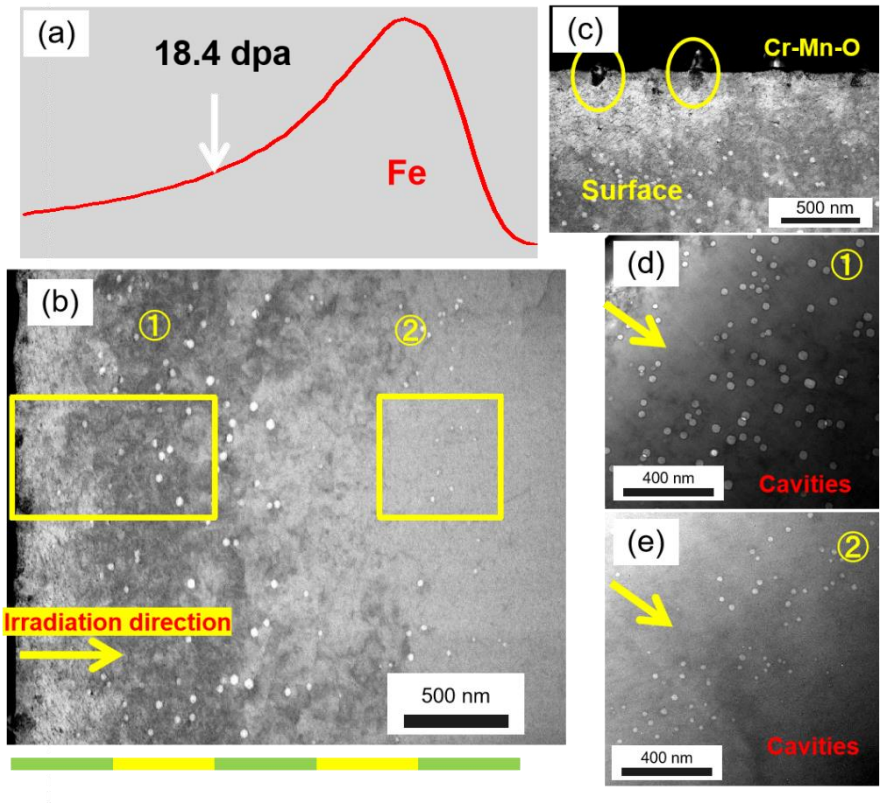

Fig 5.7 (a) Depth profile of displacement damage (dpa). (b) STEM image of single beam irradiated $Cr_{0.8}FeMnNi$. Enlarged microstructure of the surface(c), shallow region 1 (d), and deep region 2(e) of $Cr_{0.8}FeMnNi$ FIB sample.

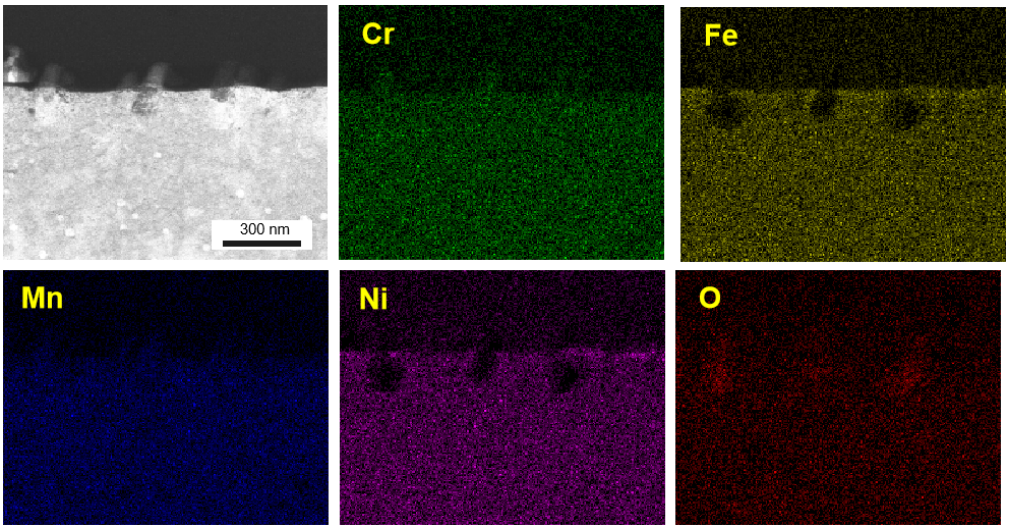

Fig 5.8 Element distribution at the surface of single beam irradiated$Cr_{0.8}FeMnNi$ using STEM-EDX method.

Fig 5.9 illustrates the microstructure at different depth of dual beam irradiated $Cr_{0.8}FeMnNi$. A similar phenomenon with single beam irradiated $Cr_{0.8}FeMnNi$ was found in Fig 5.9(c). No obvious cavity was found near the surface. Cr-Mn-O particles which are about 100 nm can be found near the surface and the composition is shown in

Fig 5.10. From 2-2.5 μm, cavities that have similar size can be found in dual beam irradiation. However, unlike single beam irradiated sample, due to the co-irradiated μm, as shown in Fig 5.9(d). Fig 5.11 illustrates the microstructure at different depth of triple beam irradiated $Cr_{0.8}FeMnNi$. Except for the thicker oxide layer formed on the surface, the microstructure is similar to dual beam irradiated samples.

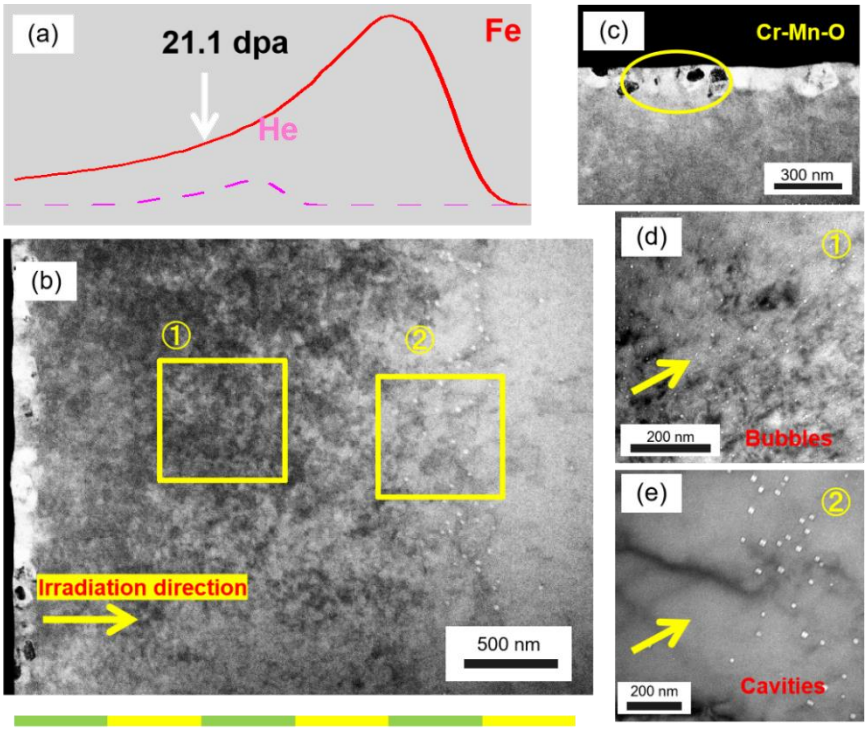

Fig 5.9 (a) Depth profile of displacement damage (dpa). (b) STEM image of dual beam irradiated $Cr_{0.8}FeMnNi$. Enlarged microstructure of the surface(c), shallow region 1 (d), and deep region 2(e) of $Cr_{0.8}FeMnNi$ FIB sample.

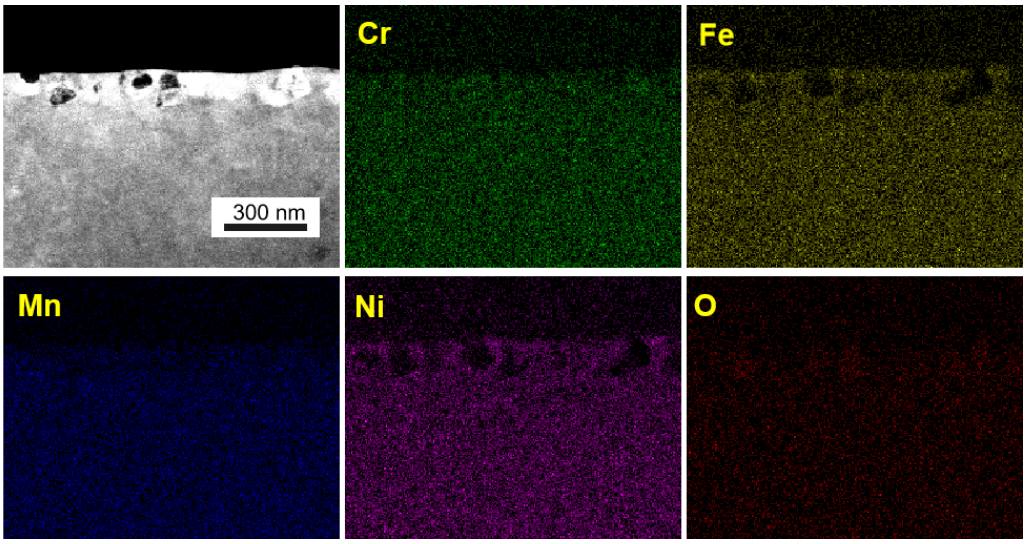

Fig 5.10 Element distribution at the surface of dual beam irradiated$Cr_{0.8}FeMnNi$ using STEM-EDX method.

The microstructure of 316L after irradiation is also investigated to compare the swelling with $Cr_{0.8}FeMnNi$. Irradiation induced dislocations with high density were also observed in 316L. As shown in Fig 5.12, unlike $Cr_{0.8}FeMnNi$, no oxide particles formed at the surface. As irradiation dose increased, some small cavities with relatively low density were found in region 2, which lies in the damage peak region. In dual and triple beam irradiated 316L, as Fig 5.13 and 5.14 show, small bubbles with high density formed in region 1, where He distributed in this region. However, in region 2, although no He was injected into this region, larger cavities formed in region 2 due to the high Fe irradiation damages.

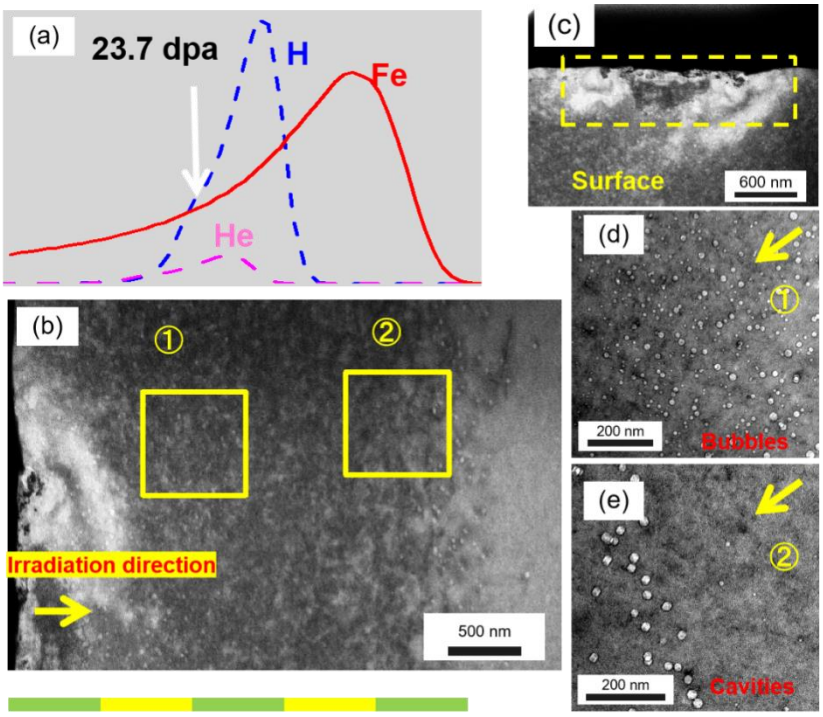

Fig 5.11 (a) Depth profile of displacement damage (dpa). (b) STEM image of triple beam irradiated $Cr_{0.8}FeMnNi$. Enlarged microstructure of the surface(c), shallow region 1 (d), and deep region 2 (e) of $Cr_{0.8}FeMnNi$ FIB sample.

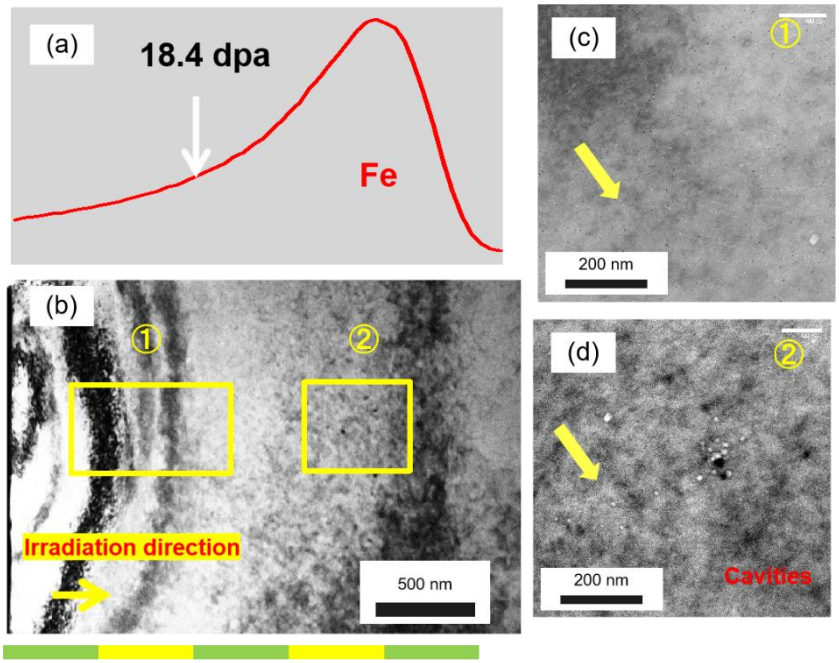

Fig 5.12 (a) Depth profile of displacement damage (dpa). (b) STEM image of single beam irradiated 316 L. Enlarged microstructure of the shallow region 1 (c), and deep region 2 (d) of 316L FIB sample.

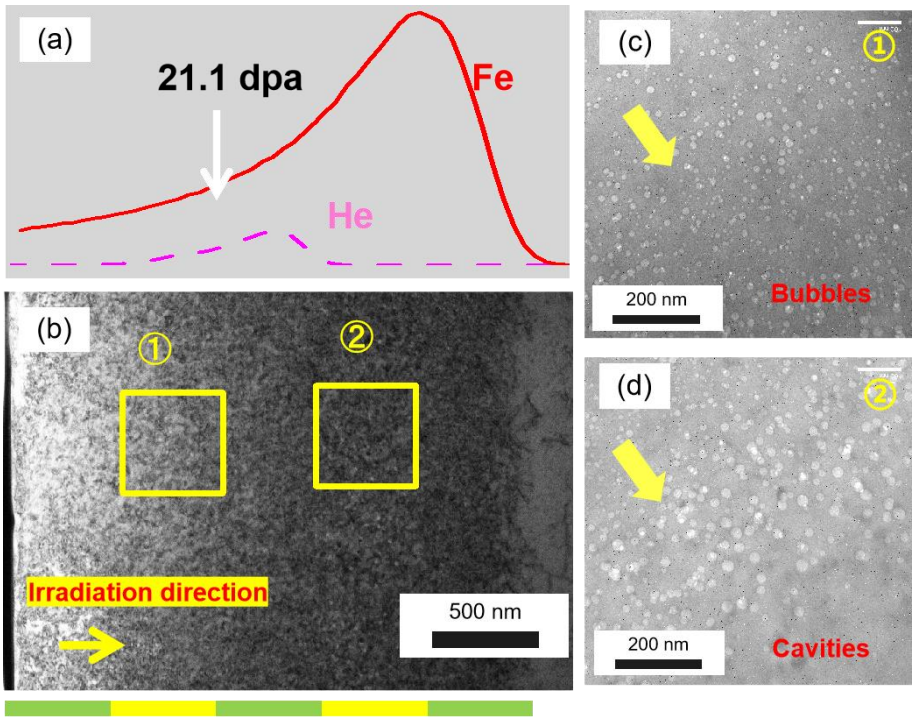

Fig 5.13 (a) Depth profile of displacement damage (dpa). (b) STEM image of dual beam irradiated $Cr_{0.8}FeMnNi$. Enlarged microstructure of the shallow region 1 (c), and deep region 2 (d) of 316L FIB sample.

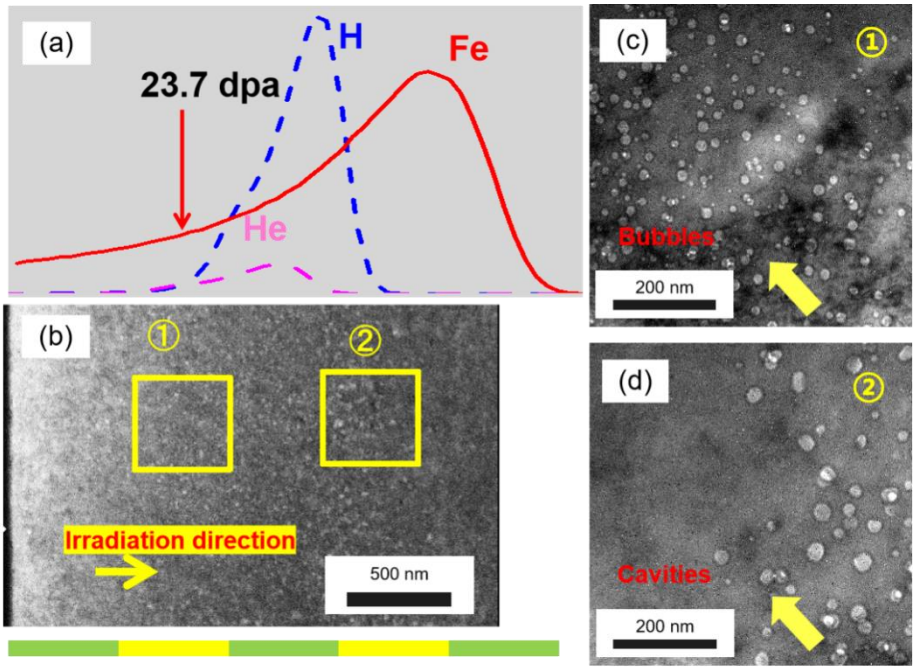

Fig 5.14 (a) Depth profile of displacement damage (dpa). (b) STEM image of triple beam irradiated $Cr_{0.8}FeMnNi$. Enlarged microstructure of the shallow region 1 (c), and deep region 2 (d) of 316L FIB sample.

To further analyze the cavities and bubble evolution, the average size and density of the voids were calculated. The irradiated region was divided into several regions with a depth of 200 nm. The statistical results are shown in Fig 5.15. The average size and density in all the irradiated samples showed bimodal distribution. Due to the surface effect, both the size and density are small in 100 nm region near the surface. In single beam irradiated samples, the first density peak appears at the depth of 0.5μm. As irradiation dose increases with the depth, the cavities grow up, showing increasing average size and decreasing density. However, both the size and density decreased at 1.5 μm. The second peak appears located at 2 μm, where the displacement damage is the highest. For dual beam and triple beam irradiated samples, the first density peak appears at 1.5 μm. As mentioned above, due to their extremely low solubility, He and H atoms tend to agglomerate into bubbles in metals [136]. In general, bubble nucleation, growth, and coarsening are controlled by the concurrent operation (including diffusion, clustering, dislocation, recombination, etc.) of He atoms, vacancies, and interstitials. As He and H injection rate increase with the depth, the size and density also increase, and the density reaches the peak at the highest He and H amount. The second peak is located at 2.5 μm, which is relatively deeper than single beam irradiated samples.

The average size and density of voids in 316L are shown in Fig 5.16. No void was

found at the surface due to the surface effect. The density of voids has the same trend as He and H distribution with depth. In both dual beam and triple beam irradiated 316L, only one density peak is found at 1.5 μm. This is due to the trapping effect of He and H on vacancies. The size of voids shows an increasing trend in total, which corresponds to the displacement damage profile.

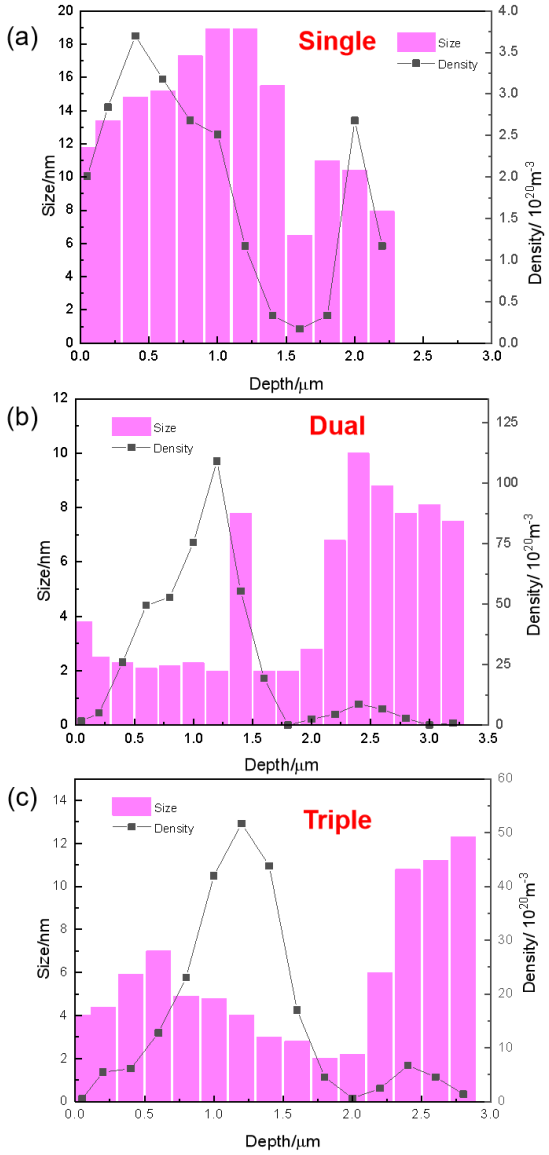

Fig 5.15 Average size and density of the voids for each region in the irradiated $Cr_{0.8}FeMnNi$.

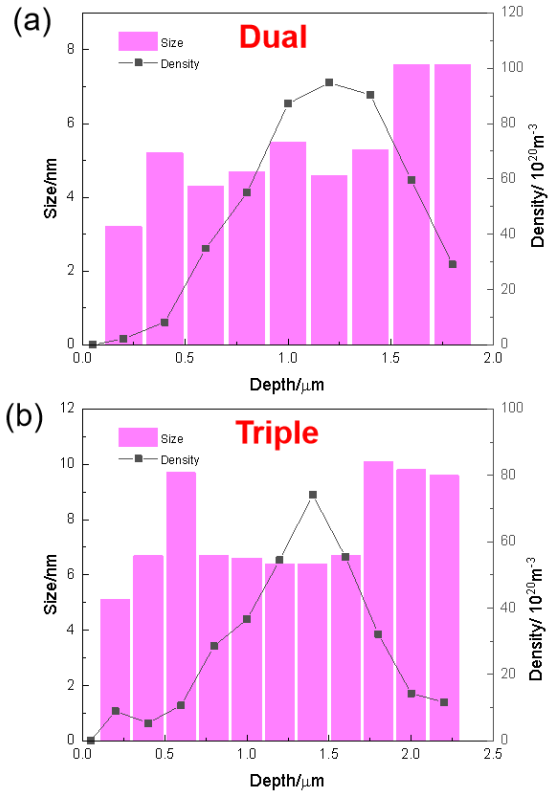

Fig 5.16 Average size and density of the voids for each region in the irradiated 316L.

5.3.3 He and H effect on microstructure evolution

To further analyze the cavities and bubble evolution, the average size and density of the voids were calculated. Fig 5.17 shows the microstructure of 316L at 1 μm. Under single beam irradiation condition, no obvious cavity was found in 316L. In dual beam and triple beam irradiated samples, small bubbles with high density was found. The bubbles in triple beam has relatively larger size and small density compared to dual beam irradiated sample.

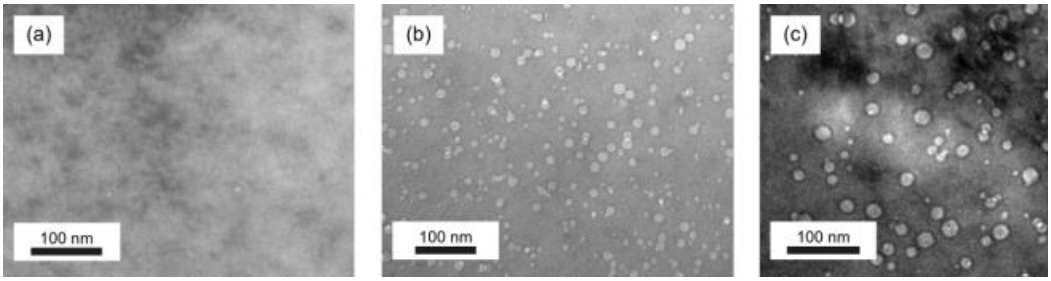

Fig 5.17 The microstructure of 316L at the depth of 1 μm under (a) single beam, (b) dual beam, and (c) triple beam irradiation.

The microstructure of $Cr_{0.8}FeMnNi$ at at 1 μm is shown in Fig 5.18. The microstructure of single beam irradiated $Cr_{0.8}FeMnNi$ showed different phenomenon from 316L. Large vacancies were found in $Cr_{0.8}FeMnNi$. In dual beam and triple beam irradiated $Cr_{0.8}FeMnNi$, the microstructure has similar phenomenon with 316L. Small bubbles with high density formed with the presence of He and H.

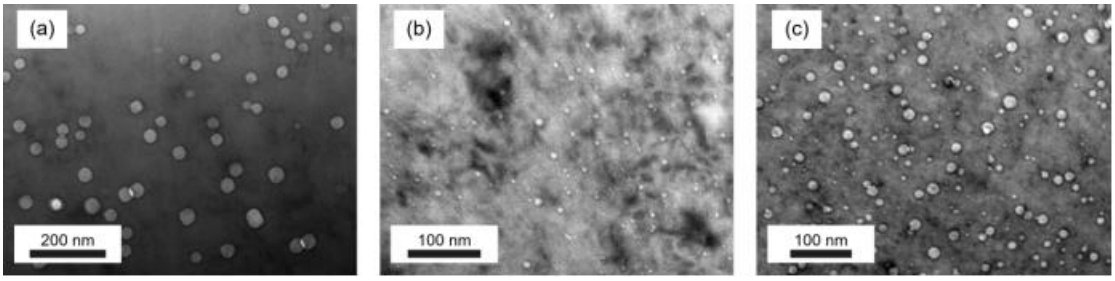

Fig 5.18 The microstructure of $Cr_{0.8}FeMnNi$ at the depth of 1 μm under (a) single beam, (b) dual beam, and (c) triple beam irradiation.

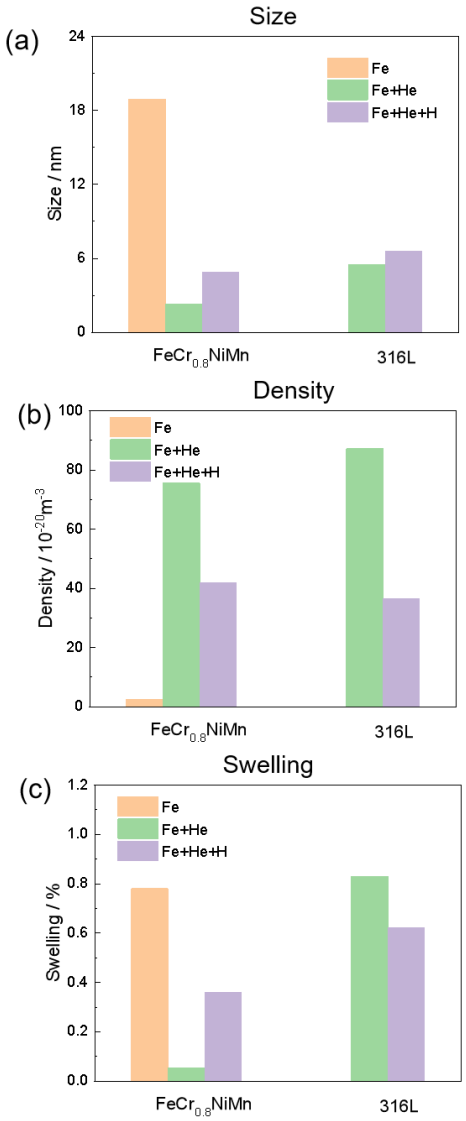

Fig 5.19 (a) The average size, (b) density of voids, and (c) swelling at 1μm of $Cr_{0.8}$FeMnNi and 316L.

The average size and density of cavities at 1μm in $Cr_{0.8}$FeMnNi and 316L are shown in Fig 5.19 (a) and (b). Under single beam irradiation, voids were found in $Cr_{0.8}$FeMnNi while no obvious cavity was observed in 316L. As discussed in last part, continuous collision cascades during irradiation induce vacancies and interstitial atoms in structure materials, which promotes formation of various defects, such as dislocation loops, voids and stacking fault tetrahedral (SFT). In addition, (*n*, α) reactions produce abundant helium (He) atoms in materials. As He has extremely low solubility in metals, it tends to accumulate and precipitate into nanoscale He bubbles in nuclear structure materials [137-139]. Irradiation temperature typically invokes a very large influence on the microstructural evolution of irradiated materials. There are several major

temperature regimes delineated by the onset of migration of point defects. At high temperature regime, the onset of vacancy motion result in the cavity formation and result in swelling [131]. Therefore, large cavities were found in single beam irradiated $Cr_{0.8}FeMnNi$. However, in the unirradiated area in 316L, dislocation lines were found after 500℃, as illustrated in Fig 5.20. Some researchers found that dislocation lines provide a defect sink so that irradiation induced interstitial atoms and vacancies tend to annihilate as a result of recombination at the dislocations. In Terasawa's work, swelling for 10% CW 316 steels is higher than that for 20% CW 316 steels and the voids in 10% CW 316 steels are larger and fewer than those in the 20% CW 316 steels [140]. Therefore, the dislocation lines existed in 316L could be the reason of the difference between single beam irradiated 316L and $Cr_{0.8}FeMnNi$.

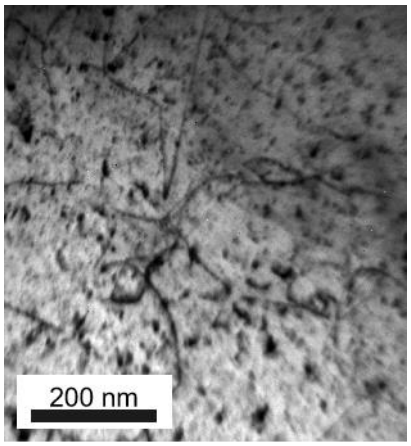

Fig 5.20 Dislocation lines in unirradiated area of single beam irradiated 316L.

In dual beam and triple beam irradiated samples, small bubbles with high density can be observed. Due to the extremely low solubility, He and H atoms tend to agglomerate into bubbles in metals [136]. In addition, as introduced in section 4, helium The low dissolution of He in the matrix and the formation of He-vacancy complexes provide nucleation cites for He bubbles. Therefore, the He can enhance the nucleation of bubbles in dual beam irradiation so that the small bubbles with higher density form in dual beam irradiated samples compared with single beam ondition.. However, both the size and density of bubbles in $Cr_{0.8}FeMnNi$ are smaller than 316L, which shows that the amount of vacancies that combined with He atoms and form stable clusters in $Cr_{0.8}FeMnNi$ is less than 316L. Therefore, the vacancy could has weaker interaction with He atoms in $Cr_{0.8}FeMnNi$.

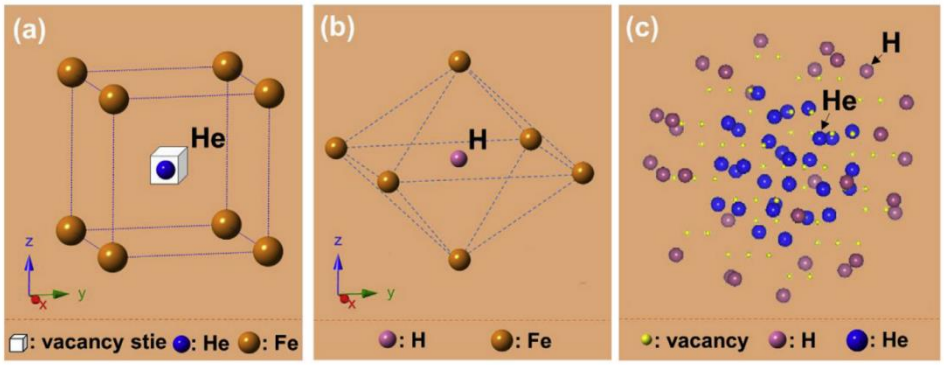

Fig 5.21 A schematic diagram of He (a), H (b) and He þ H (c) atom positions in the Fe matrix.

Under triple beam irradiation, the size of bubbles increased while the density decreased compare with dual beam irradiation in both $Cr_{0.8}$FeMnNi and 316L. In some researchers' work, the calculation result showed that the binding energy of He-vacancy complexes is larger than H-vacancy complexes [141]. Therefore, He atoms would be easily trapped by the vacancies induced during irradiation and form He-V complexes. He-vacancy complex is stable and the He atom sits in a stable substitutional position and H atom may sit in tetrahedral interstice or octahedral position as Fig 5.21 (a) and (b) shown [142]. On the other hand, the binding energy of He with the He-V complex is also larger than the binding energy of H and He-V complex for the case of monovacancy, which means the He-V complex would more easily grasp other He atoms to form He-V clusters than trap H atoms. Furthermore, He and H have only a weak van der Walls bond, but H can increase the binding of He and vacancies [143]. The addition of He allows more H to remain close to the interior of He-H-vacancy cluster with He core and H shell and also enhance H-retention in materials as Fig 5.21 (c) illustrated. Therefore, H could enhance the growth of bubbles and result in the larger size in triple beam irradiated samples.

Fig 5.19(c) illustrates the swelling of $Cr_{0.8}$FeMnNi and 316L under different irradiation conditions. Comparing the swelling of $Cr_{0.8}$FeMnNi and 316L, $Cr_{0.8}$FeMnNi shows higher swelling than 316L in single beam irradiation due to the formation of large cavities under single beam irradiation. However, the average size and density of bubbles of $Cr_{0.8}$FeMnNi under dual and triple beam irradiation are smaller than 316L. This difference can be attributed to the equi-atomic compositions in MEAs, which result in the larger lattice distortion $Cr_{0.8}$FeMnNi. This suggests a relatively higher lattice stress, which suppressed the movement of point defects. The reduced migration

of point defects in MEAs showed a synergistic effect with the trapping effect of He to vacancies largely enhanced the nucleation and prevented the growth of He bubbles. Therefore, $Cr_{0.8}FeMnNi$ showed much smaller swelling than 316L.

5.5 Summary

Four Cr-Fe-Mn-Ni MEAs $Cr_{0.65}FeMnNi$, $Cr_{0.8}FeMnNi$, $Cr_{0.8}FeMnNi_{1.3,}$ and 316L were irradiated using single, dual and triple beam. The microstructure and irradiation induced hardening effect were characterized to investigate He and H effect on MEAs.

(1) The nanoindentation test showed that MEAs showed relatively smaller hardness increment, which indicates higher irradiation hardening resistance. However, triple beam irradiated MEAs showed hardness increment. The hardness decrease might be caused by the Cr-Mn inclusion at the surface.

(2) Small bubbles with high density were found in dual and triple beam irradiated $Cr_{0.8}FeMnNi$ and 316L. He enhances the nucleation and H promotes the growth of bubbles. The interaction between He and vacancies in $Cr_{0.8}FeMnNi$ might be smaller than 316L.

(3) Although the swelling of $Cr_{0.8}FeMnNi$ under single beam irradiation at 500 ℃ is higher than 316L, $Cr_{0.8}FeMnNi$ showed excellent swelling resistance with the presence of He and H.

Chapter 6

Conclusion

Conclusions

To explore the performance of Co-free MEAs for advanced nuclear reactor application, He effect as well as H effect on the irradiation behavior of Cr-Fe-Mn-Ni MEAs were evaluated. The experimental results can be concluded as follows:

Firstly, $Cr_{0.65}FeMnNi$, $Cr_{0.8}FeMnNi$, $Cr_{0.8}FeMn_{1.3}Ni$, $Cr_{0.8}FeMn_{1.3}Ni_{1.3}$ were prepared to compare the mechanical properties. The elevated Mn content within this alloy induced a high atomic size difference within the material, inducing the highest lattice distortion in $Cr_{0.8}FeMn_{1.3}Ni$. The high lattice distortion result in highest hardness and smallest grain size, which contributing ro the high strength of $Cr_{0.8}FeMn_{1.3}Ni$.

Secondly, the in-situ irradiation experiment showed that the binding energy of the self-interstitial atom (SIA) to the He-V complex decreased as the He injection amount increased, which affect the evolution of defect evolution. The promoted defect recombination and small interstitial migrating energy result in the different size trend with increasing He injection amount.

Thirdly, $Cr_{0.8}FeMnNi$ and 316L are irradiated with single beam (Fe^{3+}), dual beam (Fe^{3+}+He^{+}), and triple beam (Fe^{3+}+He^{+}+H^{+}) at 500℃. The nanoindentation test showed that MEAs showed higher irradiation hardening resistance than 316L. He strengthens the hardening effect in $Cr_{0.8}FeMnNi$ while the hardness decreases as H is also co-irradiated. The microstructure characterization results revealed that He enhance the nucleation and H atoms promote the growth of bubbles. The interaction between He and vacancies in $Cr_{0.8}FeMnNi$ might be smaller than 316L

This work indicated that the different He injection amount can affect the point defect binding energy with He-V clusters, increasing interstitial-type defect. The bulk irradiation showed that He and H have a strong combination with vacancies, which largely affect the nucleation and the grow up of bubbles at high temperature. The interaction between He and vacancies in $Cr_{0.8}FeMnNi$ might be smaller than 316L. The synergistic effect between He and H effect and high lattice distortion in MEA reduced the swelling.

References

1. Chepeliev, M. and D. van der Mensbrugghe, Global fossil-fuel subsidy reform and Paris Agreement. Energy Economics, 2020. 85: p. 104598.

2. Lund, H., Renewable energy strategies for sustainable development. Energy, 2007. 32(6): p. 912-919.

3. Arunachalam, V. and E. Fleischer, The global energy landscape and materials innovation. MRS bulletin, 2008. 33(4): p. 264-288.

4. Zinkle, S.J. and G. Was, Materials challenges in nuclear energy. Acta Materialia, 2013. 61(3): p. 735-758.

5. EIA, U., Updated capital cost estimates for electricity generation plants. US Energy Information Administration, Office of Energy Analysis, Washington, DC, USA, 2010.

6. Holdren, J.P., Fusion Energy in Context: Its Fitness for the Long Term: A rationale for long-term energy sources suggests that some forms of fusion may be worth the wait. Science, 1978. 200(4338): p. 168-180.

7. Tanabe, T., Tritium issues to be solved for establishment of a fusion reactor. Fusion Engineering and Design, 2012. 87(5-6): p. 722-727.

8. Zinkle, S.J. and G.S. Was, Materials challenges in nuclear energy. Acta Materialia, 2013. 61(3): p. 735-758.

9. Nuclear power reactors in the world. Fuel and Energy Abstracts. Fuel and Energy Abstracts, 1995.

10. Doe, U.S., A Technology Roadmap for Generation IV Nuclear Energy Systems. http://gif.inel.gov/roadmap/pdfs/gen_iv_roadmap.pdf, 2002.

11. Zinkle, S. and N. Ghoniem, Operating temperature windows for fusion reactor structural materials. Fusion Engineering and design, 2000. 51: p. 55-71.

12. Zinkle, S.J., et al., In Space Technology and Applications International ForumSTAIF 2002 (AIP Conf. Proc. vol. 608); El-Genk, M. S., (ed.); . American Institute of

Physics: (2002), 1063., 2002.

13. Majumdar, S. and G. Kalinin, ITER structural design criteria and their extension to advanced reactor blankets. Journal of nuclear materials, 2000. 283: p. 1424-1428.

14. Yvon, P. and F. Carré, Structural materials challenges for advanced reactor systems. Journal of nuclear materials, 2009. 385(2): p. 217-222.

15. Ye, Y., et al., High-entropy alloy: challenges and prospects. Materials Today, 2016. 19(6): p. 349-362.

16. Xia, S.-q., et al., Irradiation Behavior in High Entropy Alloys. Journal of Iron and Steel Research, International, 2015. 22(10): p. 879-884.

17. Cantor, B., et al., Microstructural development in equiatomic multicomponent alloys. Materials Science and Engineering: A, 2004. 375: p. 213-218.

18. Yeh, J.W., et al., Nanostructured high-entropy alloys with multiple principal elements: novel alloy design concepts and outcomes. Advanced engineering materials, 2004. 6(5): p. 299-303.

19. Zhang, Y., et al., Microstructures and properties of high-entropy alloys. Progress in materials science, 2014. 61: p. 1-93.

20. He, J., et al., A precipitation-hardened high-entropy alloy with outstanding tensile properties. Acta Materialia, 2016. 102: p. 187-196.

21. Li, Z., et al., Interstitial atoms enable joint twinning and transformation

induced plasticity in strong and ductile high-entropy alloys. Scientific reports, 2017. 7(1): p. 40704.

22. Wang, Z., et al., The effect of interstitial carbon on the mechanical properties and dislocation substructure evolution in Fe40. 4Ni11. 3Mn34. 8Al7. 5Cr6 high entropy alloys. Acta Materialia, 2016. 120: p. 228-239.

23. Wu, Z., C. Parish, and H. Bei, Nano-twin mediated plasticity in carbon-containing FeNiCoCrMn high entropy alloys. Journal of Alloys and Compounds, 2015. 647: p. 815-822.

24. Miracle, D., Critical assessment 14: High entropy alloys and their development as structural materials. Materials Science and Technology, 2015. 31(10): p. 1142-1147.

25. Yeh, J.-W., Alloy design strategies and future trends in high-entropy alloys. Jom, 2013. 65: p. 1759-1771.

26. Lu, Z., et al., An assessment on the future development of high-entropy alloys: Summary from a recent workshop. Intermetallics, 2015. 66: p. 67-76.

27. Troparevsky, M.C., et al., Beyond Atomic Sizes and Hume-Rothery Rules: Understanding and Predicting High-Entropy Alloys. JOM, 2015. 67(10): p. 2350-2363.

28. Jien-Wei, Y., Recent progress in high entropy alloys. Ann. Chim. Sci. Mat, 2006. 31(6): p. 633-648.

29. Gludovatz, B., et al., A fracture-resistant high-entropy alloy for cryogenic applications. Science, 2014. 345(6201): p. 1153-1158.

30. Gludovatz, B., et al., Exceptional damage-tolerance of a medium-entropy alloy CrCoNi at cryogenic temperatures. Nature communications, 2016. 7(1): p. 10602.

31. El-Atwani, O., et al., Outstanding radiation resistance of tungsten-based high-entropy alloys. Science advances, 2019. 5(3): p. eaav2002.

32. Nene, S., et al., Corrosion-resistant high entropy alloy with high strength and ductility. Scripta Materialia, 2019. 166: p. 168-172.

33. Murty, B.S., et al., High-entropy alloys. 2019: Elsevier.

34. Gao, M.C., et al., High-entropy alloys: fundamentals and applications. 2016: Springer.

35. Tsai, K.Y., M.H. Tsai, and J.W. Yeh, Sluggish diffusion in Co–Cr–Fe–Mn–Ni high-entropy alloys. Acta Materialia, 2013. 61(13): p. 4887-4897.

36. Ranganathan, S., Alloyed pleasures: Multimetallic cocktails. Current science, 2003. 85(5): p. 1404-1406.

37. Li, C., et al., Neutron irradiation response of a Co-free high entropy alloy. Journal of Nuclear Materials, 2019. 527: p. 151838.

38. Chen, W.-Y., et al., Irradiation effects in high entropy alloys and 316H stainless steel at 300 C. Journal of Nuclear Materials, 2018. 510: p. 421-430.

39. Voyevodin, V., et al., Effect of irradiation on microstructure and hardening of Cr–Fe–Ni–Mn high-entropy alloy and its strengthened version. Philosophical Magazine, 2020. 100(7): p. 822-836.

40. Yang, L., et al., High He-ion irradiation resistance of CrMnFeCoNi high-entropy alloy revealed by comparison study with Ni and 304SS. Journal of Materials Science & Technology, 2019. 35(3): p. 300-305.

41. Jin, K., et al., Effects of compositional complexity on the ion-irradiation induced swelling and hardening in Ni-containing equiatomic alloys. Scripta Materialia, 2016. 119: p. 65-70.

42. Yang, T.N., The Effect of Principal Elements on Defect Evolution in Single-Phase Solid Solution Ni Alloys. 2018.

43. Zinkle, S.J. and L.L. Snead, Designing radiation resistance in materials for fusion energy. Annual Review of Materials Research, 2014. 44: p. 241-267.

44. Odette, G., M. Alinger, and B. Wirth, Recent developments in irradiation-resistant steels. Annu. Rev. Mater. Res., 2008. 38: p. 471-503.

45. Stoller, R. and G. Odette. The effect of helium on swelling in stainless steel: Influence of cavity density and morphology. in Effects of Radiation on Materials: Eleventh Int. Symp., ASTM STP. 1982.

46. Brager, H. and J. Perrin, Effects of Radiation on Materials: 11th International Symposium. 1982: ASTM International.

47. Gelles, D., Effects of irradiation on ferritic alloys and implications for fusion reactor applications. Journal of Nuclear Materials, 1987. 149(2): p. 192-199.

48. Odette, G., On mechanisms controlling swelling in ferritic and martensitic alloys. Journal of Nuclear Materials, 1988. 155: p. 921-927.

49. Maziasz, P., Overview of microstructural evolution in neutron-irradiated austenitic stainless steels. Journal of nuclear materials, 1993. 205: p. 118-145.

50. Dai, Y. and P. Marmy, Charpy impact tests on martensitic/ferritic steels after irradiation in SINQ target-3. Journal of Nuclear Materials, 2005. 343(1-3): p. 247-252.

51. Dai, Y. and W. Wagner, Materials researches at the Paul Scherrer Institute for developing high power spallation targets. Journal of nuclear materials, 2009. 389(2): p. 288-296.

52. Molvik, A., et al., A gas dynamic trap neutron source for fusion material and subcomponent testing. Fusion Science and Technology, 2010. 57(4): p. 369-394.

53. Waszczuk, P., et al., Adsorption of CO poison on fuel cell nanoparticle electrodes from methanol solutions: a radioactive labeling study. Journal of Electroanalytical Chemistry, 2001. 511(1-2): p. 55-64.

54. Kim, D., et al., Colorimetric detection and removal of radioactive Co ions using sodium alginate-based composite beads. Journal of hazardous materials, 2017. 326: p. 69-76.

55. Hosemann, P., Studying radiation damage in structural materials by using ion accelerators. Reviews of Accelerator Science and Technology, 2011. 4(01): p. 161-182.

56. Carter, D.B.W.C.B., Transmission electron microscopy A textbook for materials science. 2009.

57. Reimer, L., Transmission electron microscopy: physics of image formation and microanalysis. Vol. 36. 2013: Springer.

58. Kelly, P., et al., The determination of foil thickness by scanning transmission electron microscopy. Physica status solidi (a), 1975. 31(2): p. 771-780.

59. Sun, H., et al., Overcoming strength-ductility trade-off in CoCrNi medium entropy alloy by forming fine crescent grains in laser powder-bed fusion. Materials Letters, 2023. 347: p. 134644.

60. Kumar, N.K., et al., Microstructural stability and mechanical behavior of FeNiMnCr high entropy alloy under ion irradiation. Acta Materialia, 2016. 113: p. 230-244.

61. Wu, Y., Fusion-based hydrogen production reactor and its material selection. Journal of Nuclear Materials, 2009. 386: p. 122-126.

62. Miracle, D.B. and O.N. Senkov, A critical review of high entropy alloys and related concepts. Acta Materialia, 2017. 122: p. 448-511.

63. Zinkle, S., 1.03-Radiation-Induced effects on microstructure. Comprehensive nuclear materials, 2012. 1: p. 65-98.

64. Was, G.S., Materials degradation in fission reactors: Lessons learned of relevance to fusion reactor systems. Journal of nuclear materials, 2007. 367: p. 11-20.

65. Li, M. and S.J. Zinkle, Physical and mechanical properties of copper and copper alloys. 2012.

66. Singh, B., et al., Void swelling in copper and copper alloys irradiated with fission neutrons. Journal of nuclear materials, 1992. 191: p. 1172-1176.

67. Guo, W., et al., Dislocation-induced breakthrough of strength and ductility trade-off in a non-equiatomic high-entropy alloy. Acta Materialia, 2020. 185: p. 45-54.

68. Liu, S., et al., Stacking fault energy of face-centered-cubic high entropy alloys. Intermetallics, 2018. 93: p. 269-273.

69. Wagner, C., et al., Effects of Cr/Ni ratio on physical properties of Cr-Mn-Fe-Co-Ni high-entropy alloys. Acta Materialia, 2022. 227: p. 117693.

70. Alaneme, K.K. and E.A. Okotete, Recrystallization mechanisms and microstructure development in emerging metallic materials: A review. Journal of Science: Advanced Materials and Devices, 2019. 4(1): p. 19-33.

71. Kim, H.-C., et al., Effect of primary recrystallization texture on abnormal grain growth in an aluminum alloy. Scripta Materialia, 2007. 57(4): p. 325-327.

72. Verlinden, B., et al., Softening mechanisms. Thermo-mechanical processing of metallic materials, 2007. 11: p. 86e108.

73. Pharr, G. and W. Oliver, Nanoindentation of silver-relations between hardness and dislocation structure. Journal of Materials Research, 1989. 4: p. 94-101.

74. Chen, C. and A. Hendrickson, Dislocation etch pits in silver. Journal of Applied Physics, 1971. 42(6): p. 2208-2215.

75. Jing, Y., et al., A new proposed parameter related with atomic size effect for predicting hardness of HEA coatings. Journal of Alloys and Compounds, 2021. 856: p. 158128.

76. Otto, F., et al., Relative effects of enthalpy and entropy on the phase stability of equiatomic high-entropy alloys. Acta Materialia, 2013. 61(7): p. 2628-2638.

77. Sheng, G. and C.T. Liu, Phase stability in high entropy alloys: Formation of solid-solution phase or amorphous phase. Progress in Natural Science: Materials International, 2011. 21(6): p. 433-446.

78. Zhang, Y., et al., Solid-solution phase formation rules for multi-component alloys. Advanced engineering materials, 2008. 10(6): p. 534-538.

79. Yang, X. and Y. Zhang, Prediction of high-entropy stabilized solid-solution in multi-component alloys. Materials Chemistry and Physics, 2012. 132(2-3): p. 233-238.

80. Chen, H., et al., Contribution of lattice distortion to solid solution strengthening in a series of refractory high entropy alloys. Metallurgical and Materials Transactions A, 2018. 49: p. 772-781.

81. Sathiaraj, G.D., et al., Effect of heavy cryo-rolling on the evolution of microstructure and texture during annealing of equiatomic CoCrFeMnNi high entropy alloy. Intermetallics, 2016. 69: p. 1-9.

82. Tsai, C.-W., et al., Deformation and annealing behaviors of high-entropy alloy Al0. 5CoCrCuFeNi. Journal of Alloys and compounds, 2009. 486(1-2): p. 427-435.

83. Matsukawa, Y., et al., The effect of crystallographic mismatch on the obstacle strength of second phase precipitate particles in dispersion strengthening: bcc Nb particles and nanometric Nb clusters embedded in hcp Zr. Acta Materialia, 2016. 102: p. 323-332.

84. Shen, J., et al., Microstructural characterization and strengthening mechanisms

of a 12Cr-ODS steel. Materials Science and Engineering: A, 2016. 673: p. 624-632.

85. Kamikawa, N., et al., Stress–strain behavior of ferrite and bainite with nano-precipitation in low carbon steels. Acta Materialia, 2015. 83: p. 383-396.

86. Li, Q., Modeling the microstructure–mechanical property relationship for a 12Cr–2W–V–Mo–Ni power plant steel. Materials Science and Engineering: A, 2003. 361(1-2): p. 385-391.

87. Hornbogen, E. and E. Starke Jr, Overview no. 102 Theory assisted design of high strength low alloy aluminum. Acta metallurgica et materialia, 1993. 41(1): p. 1-16.

88. Shen, J., et al., Effects of titanium concentration on microstructure and mechanical properties of high-purity vanadium alloys. Materials & Design, 2022. 224: p. 111390.

89. Busby, J.T., M.C. Hash, and G.S. Was, The relationship between hardness and yield stress in irradiated austenitic and ferritic steels. Journal of Nuclear Materials, 2005. 336(2-3): p. 267-278.

90. Geng, D., et al., Toward the correlation of indentation hardness in micro-and nano-scale: understanding of indentation edge behaviors in Fe–Cr alloys. Journal of Materials Science, 2022. 57(28): p. 13736-13755.

91. Kashyap, B. and K. Tangri, On the Hall-Petch relationship and substructural evolution in type 316L stainless steel. Acta metallurgica et materialia, 1995. 43(11): p. 3971-3981.

92. Wu, S., et al., Strong grain-size effect on deformation twinning of an Al0. 1CoCrFeNi high-entropy alloy. Materials Research Letters, 2017. 5(4): p. 276-283.

93. Ondicho, I., B. Alunda, and N. Park, Effect of Fe on the Hall-Petch relationship of (CoCrMnNi) 100-x Fex medium-and high-entropy alloys. Intermetallics, 2021. 136: p. 107239.

94. Imrich, P.J., et al., Differences in deformation behavior of bicrystalline Cu micropillars containing a twin boundary or a large-angle grain boundary. Acta materialia, 2014. 73: p. 240-250.

95. Lu, C., et al., Enhancing radiation tolerance by controlling defect mobility and migration pathways in multicomponent single-phase alloys. Nature communications, 2016. 7(1): p. 13564.

96. Kamboj, A. and E.A. Marquis, Effect of dose rate on the phase stability of a CrFeNiMn alloy. Scripta Materialia, 2022. 215: p. 114697.

97. Huang, S., et al., Effect of He on the irradiation resistance of equiatomic CoCrFeMnNi high-entropy alloy. Journal of Nuclear Materials, 2022. 561: p. 153525.

98. Ye, F.J., et al., Helium irradiation-induced swelling resistance of heterogeneous nanoparticles in an iron-based multi-principal element alloy. Journal of Alloys and Compounds, 2023. 939: p. 168643.

99. Katoh, Y., et al., The influence of He/dpa ratio and displacement rate on microstructural evolution: a comparison of theory and experiment. Journal of nuclear materials, 1994. 210(3): p. 290-302.

100. Murakami, K., et al., Improvement of the high fluence irradiation facility at the University of Tokyo. Nuclear Instruments and Methods in Physics Research Section B: Beam Interactions with Materials and Atoms, 2016. 381: p. 67-71.

101. Allen, S.M. and E.L. Hall, Foil thickness measurements from convergent-beam diffraction patterns An experimental assessment of errors. Philosophical magazine A, 1982. 46(2): p. 243-253.

102. Li, X.-C., et al., Helium defects interactions and mechanism of helium bubble growth in tungsten: A molecular dynamics simulation. Journal of Nuclear

Materials, 2014. 451(1-3): p. 356-360.
103. Sharafat, S. and N.M. Ghoniem, Non-equilibrium agglomeration of helium-vacancy clusters in irradiated materials. Radiation effects and defects in solids, 1990. 113(4): p. 331-358.
104. Yang, J., et al. The formation energies and binding energies of helium vacancy cluster: comparative study in Ni and Pd. in Journal of Physics: Conference Series. 2006. IOP Publishing.
105. Zhang, Y., Y.N. Osetsky, and W.J. Weber, Tunable chemical disorder in concentrated alloys: defect physics and radiation performance. Chemical Reviews, 2021. 122(1): p. 789-829.
106. Oh, H.S., et al., Element-resolved local lattice distortion in complex concentrated alloys: An observable signature of electronic effects. Acta Materialia, 2021. 216: p. 117135.
107. Oh, H.S., et al., Engineering atomic-level complexity in high-entropy and complex concentrated alloys. Nature communications, 2019. 10(1): p. 2090.
108. 齋藤宏平, FCC 型 M/HEA における格子間原子の移動エネルギー. 金属学会 2023 秋, 2023.
109. Lu, Y., et al., A promising new class of irradiation tolerant materials: Ti2ZrHfV0.5Mo0.2 high-entropy alloy. Journal of Materials Science & Technology, 2019. 35(3): p. 369-373.
110. Shi, T., et al., Distinct point defect behaviours in body-centered cubic medium-entropy alloy NbZrTi induced by severe lattice distortion. Acta Materialia, 2022. 229: p. 117806.
111. Jin, K., et al., Effects of compositional complexity on the ion-irradiation induced swelling and hardening in Ni-containing equiatomic alloys. Scripta Materialia, 2016. 119: p. 65-70.
112. Zhu, T., et al., The influence of dislocation and hydrogen on thermal helium desorption behavior in Fe9Cr alloys. Journal of Nuclear Materials, 2017. 495: p. 244-248.
113. Zhao, M., et al., Effects of hydrogen isotopes in the irradiation damage of CLAM steel. Journal of Nuclear Materials, 2015. 466: p. 491-495.
114. Xu, Q., T. Yoshiie, and K. Sato, Effects of hydrogen and helium produced by transmutation reactions on void formation in copper isotopic alloys irradiated with neutrons. Journal of nuclear materials, 2009. 386: p. 363-366.
115. Shimada, M., et al., Overview of the US–Japan collaborative investigation on hydrogen isotope retention in neutron-irradiated and ion-damaged tungsten. Fusion Engineering and Design, 2012. 87(7-8): p. 1166-1170.
116. Ramachandran, R., et al., Study of defect complexes and their evolution with temperature in hydrogen and helium irradiated RAFM steel using positron annihilation spectroscopy. Fusion Engineering and Design, 2019. 142: p. 55-62.
117. Morisawa, J., et al., Hydrogen analysis and slow strain rate test in Ar gas for irradiated austenitic stainless steel. Journal of nuclear materials, 2001. 294(3): p. 241-249.
118. Kupriiyanova, Y., et al., Use of double and triple-ion irradiation to study the influence of high levels of helium and hydrogen on void swelling of 8–12% Cr ferritic-martensitic steels. Journal of Nuclear Materials, 2016. 468: p. 264-273.
119. Brimbal, D., et al., The synergistic effect of hydrogen and helium

implantations in forming H2 molecules in a Fe-12 wt.% Cr-ODS steel characterized by Raman spectroscopy and SIMS. Nuclear Instruments and Methods in Physics Research Section B: Beam Interactions with Materials and Atoms, 2019. 461: p. 191-196.

120. Zhang, R., et al., Effect of vanadium alloying on irradiation performance of tungsten under 60 keV helium irradiation. Journal of Nuclear Materials, 2018. 512: p. 65-71.

121. Singh, B., et al., Fission neutron irradiation of copper containing implanted and transmutation produced helium. Journal of nuclear materials, 1992. 191: p. 1259-1264.

122. Sato, T., T. Okita, and N. Sekimura, Effects of solid transmutation and helium on microstructural evolution in neutron-irradiated vanadium. Journal of nuclear materials, 2002. 307: p. 385-388.

123. Li, B., et al., Evaluation of helium effect on irradiation hardening in F82H, ODS, SIMP and T91 steels by nano-indentation method. Fusion Engineering and Design, 2019. 142: p. 6-12.

124. Krsjak, V., et al., Experimental comparison of the (ODS) EUROFER steels implanted by helium ions and irradiated in spallation neutron target. Journal of Nuclear Materials, 2019. 523: p. 51-55.

125. Coppola, R., et al., Micro-structural effects of irradiation temperature and helium content in neutron irradiated B-alloyed Eurofer97-1 steel. Nuclear Materials and Energy, 2018. 17: p. 40-47.

126. Gavarini, S., et al., Effects of helium irradiation on fine grained β-SiC synthesized by spark plasma sintering. Journal of the European Ceramic Society, 2020. 40(1): p. 1-11.

127. Was, G.S., et al., Emulation of reactor irradiation damage using ion beams. Scripta Materialia, 2014. 88: p. 33-36.

128. Was, G.S., et al., Emulation of neutron irradiation effects with protons: validation of principle. Journal of Nuclear Materials, 2002. 300(2): p. 198-216.

129. Zinkle, S.J. and L.L. Snead, Opportunities and limitations for ion beams in radiation effects studies: Bridging critical gaps between charged particle and neutron irradiations. Scripta Materialia, 2018. 143: p. 154-160.

130. Wakai, E., et al., Effect of helium production on swelling of F82H irradiated in HFIR. Journal of nuclear materials, 2000. 283: p. 799-805.

131. Agulló-López, F., C.R.A. Catlow, and P.D. Townsend, Point defects in materials. (No Title), 1988.

132. Budylkin, N.I., et al., Neutron-induced swelling and embrittlement of pure iron and pure nickel irradiated in the BN-350 and BOR-60 fast reactors. Journal of nuclear materials, 2008. 375(3): p. 359-364.

133. Woo, C., B. Singh, and A. Semenov, Recent advances in the understanding of damage production and its consequences on void swelling, irradiation creep and growth. Journal of nuclear materials, 1996. 239: p. 7-23.

134. Yang, T.-n., et al., Influence of irradiation temperature on void swelling in NiCoFeCrMn and NiCoFeCrPd. Scripta Materialia, 2019. 158: p. 57-61.

135. Ruault, M.-O., et al., Nucleation and growth of cobalt disilicide precipitates during in situ transmission electron microscopy implantation. Journal of Applied Physics, 2008. 104(3).

136. Li, S.-H., J.-T. Li, and W.-Z. Han, Radiation-induced helium bubbles in metals. Materials, 2019. 12(7): p. 1036.

137. Mahajan, S. and B. Eyre, Formation of dislocation channels in

neutron irradiated molybdenum. Acta Materialia, 2017. 122: p. 259-265.

138. El-Atwani, O., et al., Loop and void damage during heavy ion irradiation on nanocrystalline and coarse grained tungsten: Microstructure, effect of dpa rate, temperature, and grain size. Acta Materialia, 2018. 149: p. 206-219.

139. Kiener, D., et al., In situ nanocompression testing of irradiated copper. Nature materials, 2011. 10(8): p. 608-613.

140. Terasawa, M., S. Nakahigashi, and M. Koyama, Temperature and dose dependence of swelling in 10% and 20% cold-worked type 316 stainless steels. Journal of Nuclear Science and Technology, 1983. 20(11): p. 929-940.

141. Kirsanov, V., M. Musina, and V. Rybin, The influence of hydrogen on the formation of helium vacancy voids in metal. Journal of nuclear materials, 1992. 191: p. 1318-1322.

142. Liu, P.P., et al., Effect of helium and hydrogen synergy on vacancy migration energy in Fe-10Cr model alloy. Journal of Alloys and Compounds, 2019. 788: p. 446-452.

143. Tolstolutskaya, G.D., et al., Displacement and helium-induced enhancement of hydrogen and deuterium retention in ion-irradiated 18Cr10NiTi stainless steel. Journal of Nuclear Materials, 2006. 356(1): p. 136-147.

Academic Achievements

Journal Articles

1. **Mengke Niu**, Naoyuki Hashimoto, Hiroshi Oka, Haotian Sun. Influence of He injection amount on the microstructure of ion irradiated $Cr_{0.8}FeMnNi$ medium entropy alloy compared with 316L stainless steel[J]. Nuclear Materials and Energy, 2024, 40: 101728.
2. **Mengke Niu**, Naoyuki Hashimoto, Hiroshi Oka, Haotian Sun. Effects of Mn Content on Microstructure and Mechanical Properties of Co-Free Medium Entropy Alloys in the Cr-Fe-Mn-Ni System[J]. Materials Transactions, 2024, 65(12): 1501-1507.

Presentations on conferences

1. 2023.03, JIM 2023 spring meeting (Oral presentation).

Microstructural evolution of $Cr_{0.8}FeNiMn$ and 316L under heavy ion irradiation with He implantation.

2. 2023.07, JIM Hokkaido branch 2023 summer session (Poster).

Irradiation resistance of $Cr_{0.8}FeMnNi$ compared with 316L under single and dual beam irradiation.

3. 2023.11, JIM 2023 autumn meeting (Oral presentation).

Helium and hydrogen effect on irradiation hardening and microstructure evolution in Co-free MEA $Cr_{0.8}FeMnNi$.

4. 2023.11, Pacific Rim International Conference on Advanced Materials and Processing (Poster).

He and H effect on cavity formation and irradiation hardening on $Cr_{0.8}FeMnNi$ high entropy alloy and 316 stainless steel.

5. 2024.03, JIM 2024 spring meeting (Poster).

Influence of He-injection rate on the microstructure of ion irradiated $Cr_{0.8}FeMnNi$ medium entropy alloy compared with 316L stainless steel.

6. 2024.09, JIM 2023 autumn meeting (Oral presentation).

He and H effect on swelling behavior in ion-irradiated MEA $Cr_{0.8}FeMnNi$ compared with 316L.